

Challenge Journal of **STRUCTURAL MECHANICS**

Vol.8 No.4 (2022)

Mindlin's theory buckling columns compressive strength dynamic analysis dynamic response earthquake finite element analysis finite element method mechanical properties metaheuristic algorithms modal analysis natural frequency optimization pushover analysis reinforced concrete seismic analysis seismic design seismic isolation steel silo teaching-learning based optimization



TULPAR
ACADEMIC PUBLISHING

ISSN 2149-8024



Challenge Journal

OF STRUCTURAL MECHANICS

EDITOR-IN-CHIEF

Assoc. Prof. Dr. Fatih Mehmet ÖZKAL
Atatürk University, Türkiye

CO-EDITOR-IN-CHIEF

Assoc. Prof. Dr. Serdar ÇARBAŞ
Karamanoğlu Mehmetbey University, Türkiye

EDITORIAL BOARD

Prof. Dr. A. Ghani RAZAQPUR
McMaster University, Canada

Prof. Dr. Paulo B. LOURENÇO
University of Minho, Portugal

Prof. Dr. Gilbert Rainer GILLICH
Eftimie Murgu University of Resita, Romania

Prof. Dr. Long-Yuan LI
University of Plymouth, United Kingdom

Prof. Dr. Željana NIKOLIĆ
University of Split, Croatia

Prof. Dr. Habib UYSAL
Atatürk University, Türkiye

Prof. Dr. Filiz PİROĞLU
İstanbul Technical University, Türkiye

Assoc. Prof. Dr. Khaled MARAR
Eastern Mediterranean University, Cyprus

Assoc. Prof. Dr. Hong SHEN
Shanghai Jiao Tong University, China

Assoc. Prof. Dr. Nunziante VALOROSO
Parthenope University of Naples, Italy

Prof. Dr. Halil SEZEN
The Ohio State University, United States

Prof. Dr. Adem DOĞANGÜN
Uludağ University, Türkiye

Prof. Dr. M. Asghar BHATTI
University of Iowa, United States

Prof. Dr. Reza KIANOUSH
Ryerson University, Canada

Prof. Dr. Y. Cengiz TOKLU
Beykent University, Türkiye

Prof. Dr. Togay ÖZBAKKALOĞLU
Texas State University, United States

Prof. Dr. Mehmet ÖZYAZICIOĞLU
Atatürk University, Türkiye

Assoc. Prof. Dr. Bing QU
California Polytechnic State University, United States

Assoc. Prof. Dr. Naida ADEMOVIĆ
University of Sarajevo, Bosnia and Herzegovina

Assoc. Prof. Dr. Anna SAETTA
IUAV University of Venice, Italy

Assoc. Prof. Dr. Taha IBRAHIM <i>Benha University, Egypt</i>	Assoc. Prof. Dr. Amin GHANNADIASL <i>University of Mohaghegh Ardabili, Iran</i>
Assoc. Prof. Dr. Alper BÜYÜKKARAGÖZ <i>Gazi University, Türkiye</i>	Dr. Sandro CARBONARI <i>Marche Polytechnic University, Italy</i>
Dr. Zühal ÖZDEMİR <i>The University of Sheffield, United Kingdom</i>	Dr. Chien-Kuo CHIU <i>National Taiwan University of Science and Technology, Taiwan</i>
Dr. Syahril TAUFİK <i>Lambung Mangkurat University, Indonesia</i>	Dr. Teng WU <i>University at Buffalo, United States</i>
Dr. J. Michael GRAYSON <i>The Citadel - The Military College of South Carolina, United States</i>	Dr. Pierfrancesco CACCIOLA <i>University of Brighton, United Kingdom</i>
Dr. Fabio MAZZA <i>University of Calabria, Italy</i>	Dr. Marco CORRADI <i>University of Perugia, Italy</i>
Dr. Alberto Maria AVOSSA <i>Second University of Naples, Italy</i>	Dr. José SANTOS <i>University of Madeira, Portugal</i>
Dr. Susanta GHOSH <i>Michigan Technological University, United States</i>	Dr. Luca LANDI <i>University of Bologna, Italy</i>
Dr. Burak Kaan ÇIRPICI <i>Erzurum Technical University, Türkiye</i>	Dr. Mirko MAZZA <i>University of Calabria, Italy</i>
Dr. Panatchai CHETCHOTISAK <i>Rajamangala University of Technology Isan, Thailand</i>	Dr. Süleyman Nazif ORHAN <i>Erzurum Technical University, Türkiye</i>
Dr. Chitaranjan PANY <i>Vikram Sarabhai Space Centre, India</i>	Dr. Casim YAZICI <i>Ağrı İbrahim Çeçen University, Türkiye</i>

E-mail: cjsmec@challengejournal.com

Web page: cjsmec.challengejournal.com

TULPAR Academic Publishing
www.tulparpublishing.com





CONTENTS

Research Articles

- | | |
|---|----------------|
| Experimental study on the rotation capacity of bolted and welded beam-column connection using cold-formed steel sections | 133–140 |
| <i>Mahyar Maali, Merve Sağıroğlu, Mahmut Kılıç, Abdulkadir Cüneyt Aydın</i> | |
| Performance-based seismic design of laterally braced steel frames | 141–149 |
| <i>Sulaiman Al-Safi, Ibrahim A. Alameri, Saad Abdo Noaman Ezzedine, Muaadh Qaid Alwalidi</i> | |
| Effect of waste steel tire wired concrete on the mechanical behavior under impact loading | 150–158 |
| <i>Hasan Selim Şengel, Kutluhan Ethem Kınık, Hakan Erol, Mehmet Canbaz</i> | |
| Design and finite element analysis of a novel auxetic structure | 159–165 |
| <i>Suleyman Nazif Orhan, Şeydanur Erden</i> | |
| Boundary plate influence on tie bars axial force demands in composite plate shear walls–concrete filled | 166–172 |
| <i>Erkan Polat</i> | |
-





Research Article

Experimental study on the rotation capacity of bolted and welded beam-to-column connection using cold-formed steel sections

Mahyar Maali ^{a,*} , Merve Sağiroğlu ^a , Mahmut Kılıç ^b , Abdulkadir Cüneyt Aydın ^b

^a Department of Civil Engineering, Erzurum Technical University, 25050 Erzurum, Türkiye

^b Department of Civil Engineering, Atatürk University, 25240 Erzurum, Türkiye

ABSTRACT

This paper investigates new bolted and welded beam-to-column connection types on the cold-formed steel sections (CFS) and their behaviors determined using full-scale experiments. This study aimed to analyze the influence of weld/bolt connections based on CFS profile and failure modes to provide the necessary data for improving Eurocode 3. In contrast, the rotation and ductility of a joint of the welded connection are lower than the bolted connection. Thus, the bolted connection exhibits a semi-rigid behavior—also, the energy dissipation capacity values in the bolted connection are bigger than welded connection. Thus, the bolted connection has a semi-rigid behavior. Also, model failure is determined by the type of connection (bolted and welded). The rotation and ductility of a joint of the welded connection are lower than the bolted connection. Thus, the bolted connection exhibits a semi-rigid behavior—also, the energy dissipation capacity values in the bolted connection are bigger than welded connection. Furthermore, the specimens of the welded connection have rigid behavior in the failure modes.

ARTICLE INFO

Article history:

Received 21 April 2022

Revised 13 May 2022

Accepted 9 June 2022

Keywords:

Experimental study
Moment–rotation curves
CFS profile
Weld/bolt connection
Eurocode 3

1. Introduction

The use of light steel in a structural system has been increasing rapidly in recent years because of many advantages such as being economical, faster construction, and lightness. However, the existing design guides concerning domestic and foreign standards are not as straightforward as those of conventional steel structures. The most important area in steel column beam elements is the connection area. In addition, connecting tools are made in light steel (cold-formed steel) with various methods (bolt, weld, and screw). It is necessary to consider the behavior of connections in the design and analysis of steel frames because it represents the actual behavior (Sagiroglu and Aydın 2015). Beam-column connections are considered rigid or pinned in traditional steel structures calculation methods. Although this idealization of the joint behavior simplifies the analysis process, it results in differences between the idealized behavior and the actual behavior of the structure. According to these theoretical idealizations;

- In rigid connections, there is no local rotation in the elements; when an external moment acts, this moment is distributed in proportion to the stiffness of the elements.
- Again, according to this assumption, local rotation occurs in an articulated joint. However, the elements do not transfer moment.

However, the joints are neither perfectly rigid nor fully articulated in reality. Joints used in steel frames exhibit semi-rigid and non-linear behavior. In recent studies, it has been proven that accepting the joint as semi-rigid gives more accurate results. In addition, some studies have shown that semi-rigid joint performance provides benefits such as reduction in joint elements, size, and weight (Bagheri et al. 2012). Fig. 1 shows the behavior of the steel beam to column connection.

Recently, many experimental studies have been carried out to examine the actual behavior of cold-formed steel beam-column connections. However, after 1950, experimental studies focused on semi-rigid connections. Therefore, cold-formed steel beam-to-column connec-

* Corresponding author. Tel.: 444-5-388 ; Fax: +90-442-230-0036 ; E-mail address: mahyar.maali@erzurum.edu.tr (M. Maali)

tions types investigated in recent years have increased, and many researchers are trying to obtain the actual behavior of the connection. In addition, experimental research on this topic is limited due to the high cost of experimenting. Therefore, both numerical and experi-

mental studies in the literature are examined, and it is seen that the effort to obtain the actual behavior on these issues is limited. Table 1 summarizes the cold-formed steel beam-to-column connections experiments performed in the last ten years.

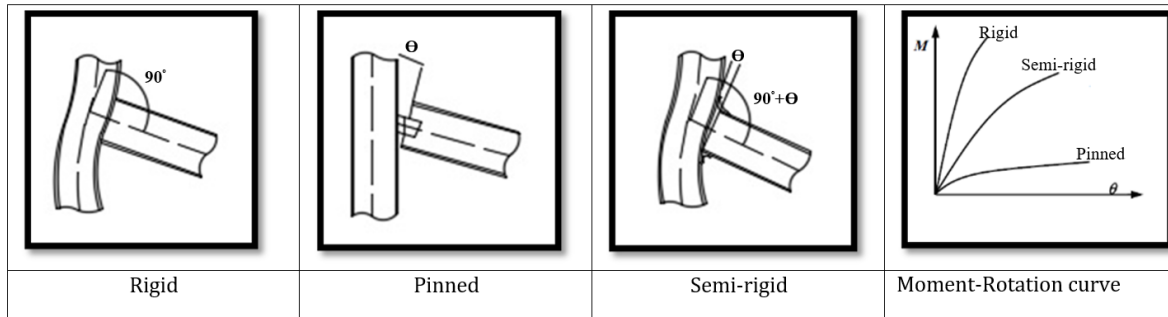


Fig. 1. Joint types.

Table 1. Cold-formed beam-to column connection experiments.

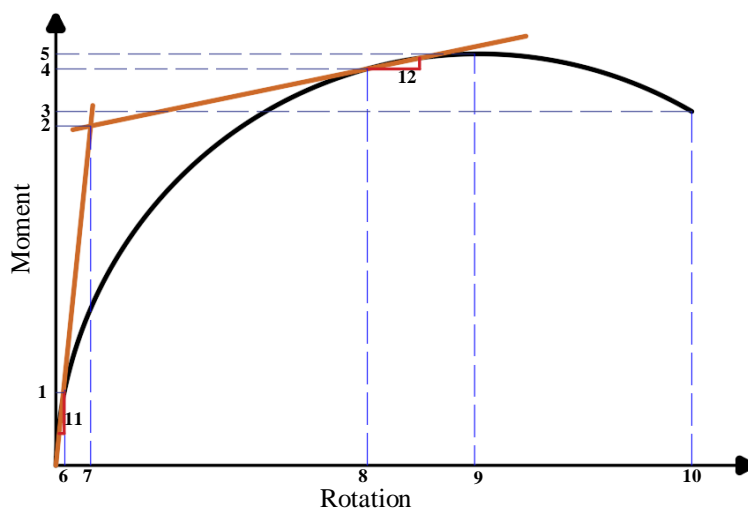
Author	Aim of research (CFS)	Number of experiments
Bagheri et al. (2012)	Moment resistance determined by the earthquake	3
Anwer et al. (2012)	Bolted connections for the channel sections	10
Torabian et al. (2015)	Lipped channel	20
Freya et al. (2016)	Semi rigid connections	2
Serror et al. (2016)	Rotation capacity	10
Maali et al. (2018a9)	Screwed beam-to-column connections	3
Zhao et al. (2018)	Hysteretic behaviour of steel storage rack beam-to-upright boltless connections	8
Bucmys et al. (2018)	Bolted gusset plate joints	3
Ayhan and Schafer (2019)	Floor-to-wall connection	27
Benchaphong et al. (2021)	Bolted connection in the trusses	9

In this research, the beam-to-column connection of endplate and double C profile beam jointed with gusset plate and bolted and welded was selected. The moment rotation ($M-\theta$) behavior, moment-rotation characteristic values, and failure modes of the bolted and welded beam-to-column connections in the cold-formed steel structures with various dimensions of elements have been evaluated and compared. Various beam thicknesses and gusset plate thicknesses have been used to make a meaningful comparison. Also, the welded group was compared to bolted group specimens tests. Six cold-formed steel connections in two groups (welded and bolted) have been tested based on these parameters. Finally, this paper presents the evolutionary development to use bolted-welded connections by beginning by using different beams and different gusset plate thicknesses.

2. Specimens Test Details

This paper presents the six experimental tests in two groups that studied the rotation capacity of bolted and welded beam-column connections using cold-formed

steel sections under statically loaded. All experiments were done on a 1/1 scale. The experimental program is shown in Fig. 2 and detailed in Table 2. First, the gusset plate with various thicknesses was welded (the manual metal arc welding process) to the end plate with a thickness equal to 10 mm using a continuous 45° fillet weld with the down-hand position for the workshop (Aydın et al. 2015a, 2015b; Maali et al. 2015). Second, the stiffener with 2mm thicknesses was welded to the C Profile. The gusset plate CFS profile, plate stiffener, and end-plate properties were S235. The weld length was 50mm with 2mm weld thickness in the weld group specimens test. The bolt's diameter was M8 with grade 8.8. The beam is made of back-to-back light steel channel sections composed of 13 bolts, and the beam-to-column connection was a connection area with nine bolts. Thus, this study aimed to analyse the influence of various beam thicknesses and used stiffener in the CFS beams, with gusset plate with various thicknesses on the behavior of moment-rotation curve, to provide the necessary data for improving Eurocode 3 (Eurocode 3 2005) and also, compare the moment-rotation curves results of the experiments in the welded group and the test results in the bolted group.



1. Lower moment in the elastic area, $M_{\min k-R}$
2. The plastic flexural resistance, $M_{j,Rd}$
3. The bending moment capacity, $M_{\theta,Cd}$
4. Upper moment in the plastic area, $M_{\sup k-R}$
5. The maximum bending moment, $M_{j,max}$
6. The rotation lower moment in the elastic area, $\theta_{\min k-R}$
7. The rotation plastic flexural resistance, $\theta_{M,Rd}$
8. The rotation upper moment in the plastic area, $\theta_{\sup k-R}$
9. The rotation maximum bending moment, $\theta_{M,j,max}$
10. The rotation capacity, θ_{Cd}
11. The initial stiffness, $S_{j,ini}$
12. Post-limit stiffness, $S_{j,p-1}$

Fig. 3. Moment-rotation curve characteristics of the Eurocode 3.

4. Test Results

In this study, the moment-rotation curves of six cold-formed steel beam-to-column under static load are drawn, and characteristic features such as moment re-

sistance, stiffness, rotation capacity, the ductility of a joint, and energy dissipation are represented by moment-rotation curves are determined. Fig. 4 and Table 3 show the moment-rotation characteristics of the two groups.

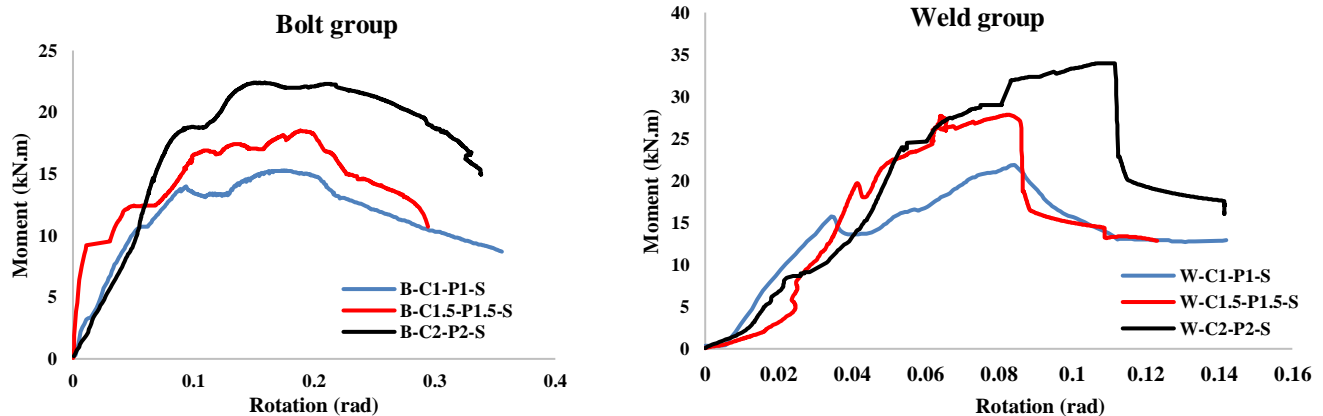


Fig. 4. Moment-rotation curve of the two group.

Table 3. Moment-rotation characteristic properties for all specimens' tests.

Group	Experiment	Resistance (kN.m)			Stiffness (kN m/rad)			Rotation (rad)			Ductility of a joint		Energy dissipation (kN.m.rad)
		$M_{j,Rd}$	$M_{j,max}$	$M_{j,max}/M_{j,Rd}$	$S_{j,ini}$	$S_{j,p-1}$	$S_{j,ini}/S_{j,p-1}$	$\theta_{Mj,Rd}$	$\theta_{Mj,max}$	θ_{Cd}	$\Psi_j = \frac{\theta_{Cd}}{\theta_{Mj,Rd}}$	$\Psi_{j,maxload} = \frac{\theta_{Mj,max}}{\theta_{Mj,Rd}}$	
Bolt	B-C1-P1-S	13.42	15.28	1.14	0.38	3.87	0.098	0.065	0.17	0.35	5.39	2.62	3.41
	B-C1.5-P1.5-S	14.22	18.39	1.29	0.14	4.16	0.033	0.031	0.191	0.29	9.35	6.16	3.89
	B-C2-P2-S	21.03	22.37	1.06	0.59	7.36	0.08	0.103	0.15	0.34	3.30	1.46	4.14
Weld	W-C1-P1-S	16.80	21.83	1.30	0.58	2.91	0.199	0.036	0.08	0.141	3.91	2.22	0.98
	W-C1.5-P1.5-S	22.78	27.61	1.21	0.46	2.56	0.18	0.044	0.08	0.123	2.80	1.82	1.82
	W-C2-P2-S	29.07	32.71	1.12	1.1	7.72	0.142	0.071	0.11	0.14	1.97	1.55	2.57

4.1. Bolt group

Fig. 4 and Table 3 show that the plastic flexural resistance and the maximum bending moment values increased by about 5.6%–36.18% and 16.91%–31.69%, respectively, with increased gusset plate thicknesses and beam thicknesses of the 1mm to 2mm. Also, the ideal value for the $M_{j,max}/M_{j,Rd}$ is between 1 and 1.3. Table 3 shows that the $M_{j,max}/M_{j,Rd}$ for the B-C1.5-P1.5-S and B-C1-P1-S specimens test increased by about 11.62%, increasing beam thicknesses and gusset thickness of 1 to 1.5mm. While, the $M_{j,max}/M_{j,Rd}$ for the between B-C2-P2-S and B-C1-P1-S and between B-C2-P2-S and B-C1.5-P1.5-S specimens test decreased by about 7.55% and 21.70%, respectively, with an increase in beam thicknesses and gusset thicknesses. Table 3 shows that the $S_{j,ini}/S_{j,p-1}$ values decreased by about 22.5%–196.97%, respectively, with increased gusset plate thicknesses and beam thicknesses of 1mm to 2mm. Additionally, Table 3 shows that the θ_{MjRd} value for B-C1.5-P1.5-S and B-C1-P1-S specimens test decreased by about 109.67%, increasing beam thicknesses and gusset thicknesses of the 1 to 1.5mm. While the θ_{MjRd} value for the between B-C2-P2-S and B-C1-P1-S and between B-C2-P2-S and B-C1.5-P1.5-S specimens test increased by about 36.89% and 69.90%, respectively, with an increase in beam thicknesses and gusset thicknesses. Moreover, Table 3 shows that $\theta_{Mj,max}$ value for the B-C1.5-P1.5-S and B-C1-P1-S specimens test increased by about 10.99%, increasing beam thicknesses and gusset thicknesses of the 1 to 1.5mm. While the $\theta_{Mj,max}$ value for the between B-C2-P2-S and B-C1-P1-S and between B-C2-P2-S and B-C1.5-P1.5-S specimens test decreased by about 13.33% and 27.33%, respectively, with an increase in beam and gusset thicknesses. In addition, Table 3 shows that θ_{Cd} value for the B-C2-P2-S, B-C1.5-P1.5-S, and B-C1-P1-S specimens test decreased by about 20.68%–2.94% with an increase in beam thicknesses and gusset thicknesses of the 1 to 2mm. Also, Table 3 shows that the Ψ_j for the B-C1.5-P1.5-S and B-C1-P1-S specimens test increased by about 42.35%, with an increase in beam thicknesses and gusset thicknesses of the 1 to 1.5mm. While, the Ψ_j for the between B-C2-P2-S and B-C1-P1-S and between B-C2-P2-S and B-C1.5-P1.5-S specimens test decreased by about 63.33% 183.33%, respectively, with an increase in beam thicknesses and gusset thicknesses. Moreover, Table 3 shows that the $\Psi_{j,maxload}$ for the B-C1.5-P1.5-S and B-C1-P1-S specimens test increased by about 57.46%, with an increase in beam thicknesses and gusset thicknesses of the 1 to 1.5mm. While, the $\Psi_{j,maxload}$ for the between B-C2-P2-S and B-C1-P1-S and between B-C2-P2-S and B-C1.5-P1.5-S specimens test decreased by about 79.45% and 321.92%, respectively, with an increase in beam thicknesses and gusset thicknesses. Also, the energy dissipation capacity increased by about 12.33%–17.63% with an increase in beam thicknesses and gusset thicknesses of 1 to 2mm. Generally, the moment resistance, critical rotation capacity, and energy dissipation capacity increased with an increase in beam thicknesses and gusset thicknesses of 1 to 2mm. While the stiffness decreased with an increase in beam thicknesses and gusset thicknesses of 1 to 2mm.

4.2. Weld group

Fig. 4 and Table 3 show that the plastic flexural resistance and the maximum bending moment values increased by about 26.25%–42.21% and 20.93%–33.26%, respectively, with increased gusset plate thicknesses and beam thicknesses of the 1mm to 2mm. Also, the $S_{j,ini}/S_{j,p-1}$ values decreased by about 10.55%–40.14%, respectively, with increased gusset plate thicknesses and beam thicknesses of 1mm to 2mm. Also, the θ_{MjRd} value increased by about 18.18%–49.29%, increasing beam thicknesses and gusset thicknesses of 1 to 2mm. Moreover, the $\theta_{Mj,max}$ value increased by about 27.27% with an increase in beam thicknesses and gusset thicknesses 1 to 2mm. While the θ_{Cd} value decreased by about 0.71%–14.63% with an increase in beam thicknesses and gusset thicknesses of 1 to 2mm. In addition, Table 3 shows that the Ψ_j and $\Psi_{j,maxload}$ values decreased by about 39.64%–194% and 21.97%–43.22%, respectively, with an increase in beam thicknesses and gusset thicknesses of the 1 to 2mm. Also, the energy dissipation capacity increased by about 19.71%–30.08% with an increase in beam thicknesses and gusset thicknesses of 1 to 2mm. Generally, the moment resistance, plastic flexural rotation capacity, and maximum rotation capacity increased with beam thicknesses and gusset thicknesses of 1 to 2mm. While the stiffness, critical rotation capacity, energy dissipation capacity, and the ductility of a joint decreased with an increase in beam thicknesses and gusset thicknesses of 1 to 2mm.

4.3. Comparison between bolt and weld group

Fig. 5 and Table 4 show the comparison between bolt and weld groups. Fig. 5 and Table 4 show the following:

- The $M_{j,Rd}$, $M_{j,max}$ and $S_{j,ini}/S_{j,p-1}$ values for the W-C1-P1-S and B-C1-P1-S, W-C1.5-P1.5-S and B-C1.5-P1.5-S, W-C2-P2-S and B-C2-P2-S models increased by about 20.12%, 37.57%, 27.66%, 30%, 33.39%, 31.61%, 50.75%, 81.66%, and 43.66%, respectively, with used welded connection compared to bolted connection. Therefore, the welded connection exhibits a rigid behavior.
- The θ_{MjRd} , $\theta(M_{j,max})$, θ_{Cd} , Ψ_j and $\Psi_{j,maxload}$ values for the W-C1-P1-S and B-C1-P1-S, W-C1.5-P1.5-S and B-C1.5-P1.5-S, W-C2-P2-S and B-C2-P2-S models decreased by about 80.55%, 45.07%, 112.5%, 138.8%, 36.36%, 148.22%, 135.77%, 142.86%, 37.85%, 233.93%, 67.52%, 18.01%, and 238.46%, respectively, with used welded connection compared to bolted connection. While, The θ_{MjRd} , and $\Psi_{j,maxload}$ values for the W-C1.5-P1.5-S and B-C1.5-P1.5-S, W-C2-P2-S and B-C2-P2-S models increased by about 29.55%, and 5.81%, respectively, with used welded connection compared to bolted connection. Hence, the rotation and ductility of a joint of the welded connection lower than the bolted connection. Thus, The bolted connection exhibits a semi-rigid behavior.
- The energy dissipation capacity values for the W-C1-P1-S and B-C1-P1-S, W-C1.5-P1.5-S and B-C1.5-P1.5-S, W-C2-P2-S and B-C2-P2-S models decreased by about -247.96%, -113.74% and -61.09%, respectively.

tively, with used welded connection compared to bolted connection. Therefore, the energy dissipation capacity values in the bolted connection are bigger than welded connection. Thus, the bolted connection has a semi-rigid behavior.

Generally, the rotation and ductility of a joint of the welded connection are lower than the bolted connection. Thus, the bolted connection exhibits a semi-rigid behaviour also, the energy dissipation capacity values in the bolted connection are bigger than welded connection. Thus, the bolted connection has a semi-rigid behavior.

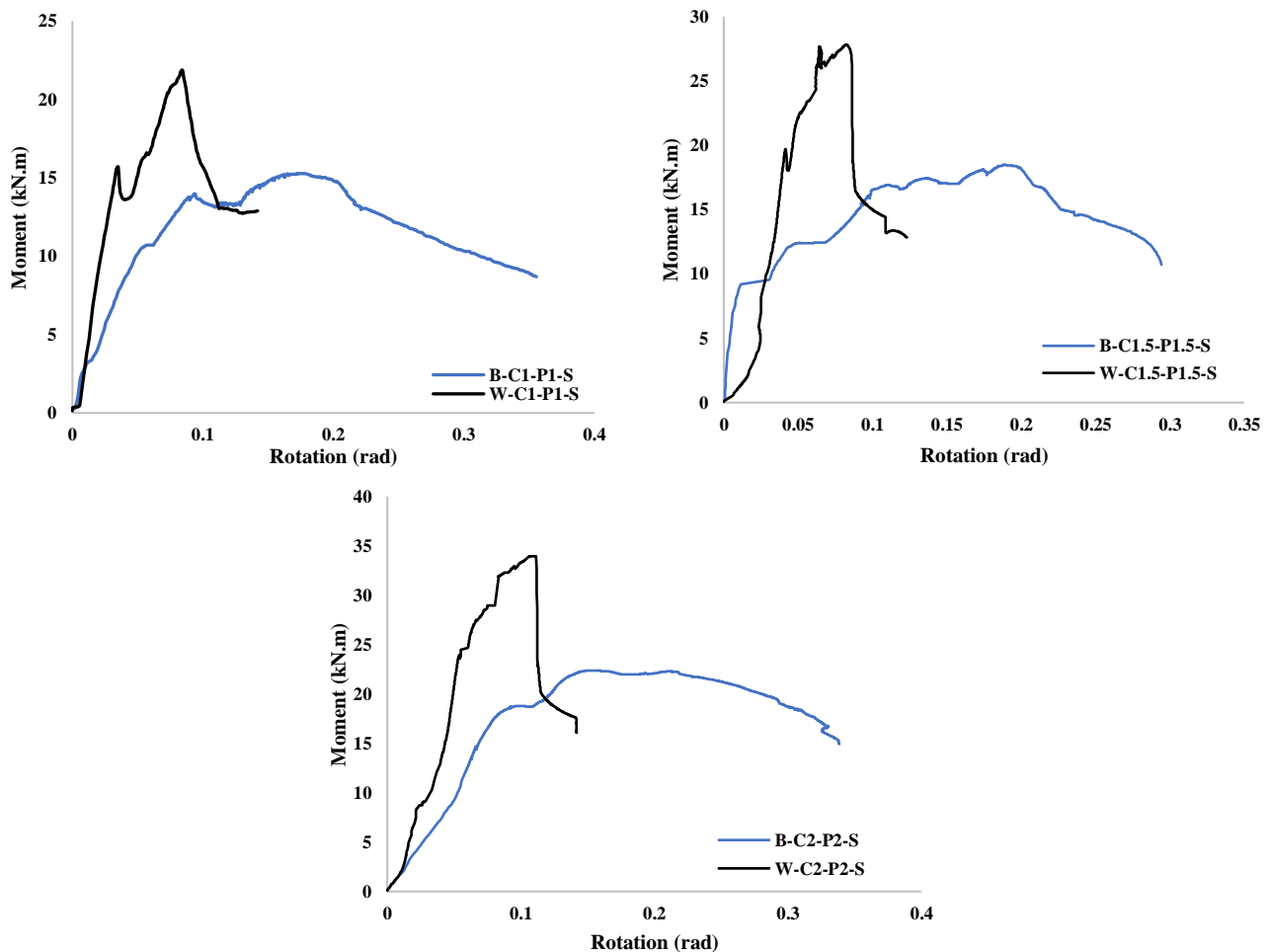


Fig. 5. The moment-rotation characteristics comparison between test specimens.

Table 4. The moment-rotation characteristics comparison for all test specimens.

Experiment	$M_{j,Rd}$	$M_{j,max}$	$S_{j,ini}/S_{j,p}^{-1}$	$\theta_{Mj,Rd}$	$\theta_{Mj,max}$	θ_{Cd}	Ψ_j	$\Psi_{j,maxload}$	Energy Dissipation
Percent W-C1-P1-S to B-C1-P1-S (%)	20.12	30.00	50.75	-80.55	-112.50	-148.22	-37.85	-18.01	-247.96
Percent W-C1.5-P1.5-S to B-C1.5-P1.5-S (%)	37.57	33.39	81.66	29.55	-138.80	-135.77	-233.93	-238.46	-113.74
Percent W-C2-P2-S to B-C2-P2-S (%)	27.66	31.61	43.66	-45.07	-36.36	-142.86	-67.52	5.81	-61.09

4.4. Failure modes

Fig. 6 shows the test specimens' collapse modes. There are three types of failure modes for bolted connections in Eurocode 3 (1993); there are three types of failure modes the first is only plate yielding, the second is plate yielding with bolt breakage, and the third is only bolt breakage. Therefore, comparisons of failure modes were made as

follows, according to Fig. 6: in the bolt's connection specimens test, all specimens' tests. The collapse occurred with the yield gusset plate with tear gusset. Also, all models were without the bolts failing, and the shape of the gusset plate after it collapsed was similar to the sinus shape. Thus, failure modes in the bolted connection occurred in the second mode in Eurocode 3 (1993). In the welded connection specimens test, in the all-specimens tests, the col-

lapse occurred with the yield gusset plate with the sharing welding in the end-plate area. Also, all model collapse occurred with the buckled C profile beam. Generally, model

failure is determined by the type of connection (bolted and welded). Furthermore, the specimens of the welded connection have rigid behavior in the failure modes.



Fig. 6. Collapse modes of test specimens and comparing collapse mode.

5. Conclusions

The aim of this study was studied on the rotation capacity of bolted and welded beam-column connections using cold-formed steel sections. The main conclusions can be summarized as follows:

- Bolted connection: the moment resistance, critical rotation capacity, and energy dissipation capacity increased with beam thicknesses and gusset thicknesses of 1 to 2mm. In contrast, the stiffness decreased with an increase in beam thicknesses and gusset thicknesses of 1 to 2mm.

- Welded connection: the moment resistance, plastic flexural rotation capacity, and maximum rotation capacity increased with beam thicknesses and gusset thicknesses of 1 to 2mm. While the stiffness, critical rotation capacity, energy dissipation capacity, and the ductility of a joint decreased with an increase in beam thicknesses and gusset thicknesses of 1 to 2mm.
- Comparison between bolt and weld group: the rotation and ductility of a joint of the welded connection lower than the bolted connection. Thus, the bolted connection exhibits a semi-rigid behaviour also, the energy dissipation capacity values in the bolted connection are bigger than welded connection. Thus, the bolted connection has a semi-rigid behavior.
- Failure modes: model failure is determined by the type of connection (bolted and welded). Furthermore, the specimens of the welded connection have rigid behavior in the failure modes.

Acknowledgements

None declared.

Funding

The authors received no financial support for the research, authorship, and/or publication of this manuscript.

Conflict of Interest

The authors declared no potential conflicts of interest with respect to the research, authorship, and/or publication of this manuscript.

REFERENCES

- Anwer B, Saad S, Osman H (2012). Structural performance of bolted moment connections among single cold-formed channel sections. *International Journal of Engineering and Technology*, 2(4), 599-607.
- Aydin AC, Maali M, Kiliç M, Sağiroğlu M (2015a). Experimental investigation of sinus beams with end-plate connections. *Thin-Walled Structure*, 97, 35-43.
- Aydin AC, Kiliç M, Maali M, Sağiroğlu M (2015b). Experimental assessment of the semi-rigid connections behavior with angles and stiffeners. *Journal of Constructional Steel Research*, 114, 338-348.
- Ayhan D, Schafer BW (2019). Cold-formed steel ledger-framed construction floor-to-wall connection behavior and strength. *Journal of Constructional Steel Research*, 156, 215-226.
- Bagheri SA, Petkovski M, Pilakoutas K, Mirghaderi R (2012). Development of cold-formed steel elements for earthquake resistant moment frame buildings. *Thin-Walled Structures*, 53, 99-108.
- Benchaphong A, Hongthong R, Benchanukrom S, Konkong N (2021). Stiffness prediction for bolted moment-connections in cold-formed steel trusses. *Engineering Review*, 41(1), 69-84.
- BS EN 1993-1-8 (2005). Eurocode 3. Design of Steel Structures Design of Joints.
- Buřmys Ž, Daniūnas A, Jaspart JP, Demonceau JF (2018). A component method for cold-formed steel beam-to-column bolted gusset plate joints. *Thin-Walled Structures*, 123, 520-527.
- Freya R, Senthil R, Merin WJ, Saravanakumar R, Kuber K, Gowtham M (2016). Behaviour of cold-formed steel semi rigid connections. *Wei-Wen Yu International Specialty Conference on Cold-Formed Steel Structures*, 4.
- Kılıç M, Maali M, Aydın AC (2019). The preliminary uniaxial compression behavior of corrugated cold formed steel members. *Architecture Civil Engineering, Environment*, 12(2), 105 - 116
- Maali M (2018). Dikey berkitmeli alın levhalı kiriş-kolon birleşimlerin davranışının deneysel olarak incelenmesi. *Gümüşhane University Journal of Science and Technology*, 8(2), 255-263. (in Turkish)
- Maali M, Aydın AC, Sağiroğlu M (2015). Investigation of innovative steel runway beam in industrial building. *Sadhana*, 40(7), 2239-2251.
- Maali M, Sağiroğlu M, Solak MS (2018a). Experimental behavior of screwed beam-to-column connections in cold-formed steel frames. *Arabian Journal of Geosciences*, 11(9), 1-6.
- Maali M, Kiliç M, Sağiroğlu M, Aydın AC (2018b). Experimental behavior of bolted t-stub connections with IPE standard profile. *Journal of Civil & Environmental Engineering*, 8(3), 1-8.
- Maali M, Kiliç M, Aydın AC (2019). Experimental behaviour of bolted connections with stiffeners. *Steel Construction*, 12(2), 105-113.
- Sağiroğlu M, Aydın AC (2015). Design and analysis of non-linear space frames with semi-rigid connections. *Steel and Composite Structures*, 18(6), 1405-1421.
- Serror MH, Hassan EM, Mourad SA (2016). Experimental study on the rotation capacity of cold-formed steel beams. *Journal of Constructional Steel Research*, 121, 216-228.
- Torabian S, Zheng B, Schafer BW (2015). Experimental response of cold-formed steel lipped channel beam-columns. *Thin-Walled Structures*, 89, 152-168.
- Zhao Z, Dai L, Rasmussen KJR (2018). Hysteretic behaviour of steel storage rack beam-to-upright boltless connections. *Journal of Constructional Steel Research*, 144, 81-105.



Research Article

Performance-based seismic design of laterally braced steel frames

Sulaiman Al-Safi ^a , Ibrahim A. Alameri ^{a,b,*} ,

Saad Abdo Noaman Ezzedine ^a , Muaadh Qaid Alwalidi ^a

^a Department of Civil Engineering, Sana'a University, 13341 Sana'a, Yemen

^b Department of Civil Engineering, Atatürk University, 25240 Erzurum, Türkiye

ABSTRACT

Improving the performance of structural frames is one of the most important focuses of today's researchers. The total base shear capacity of the structural frames will increase by reaching the maximum number of plastic hinges. In this work, the effects of bracing system type on different heights of steel frames were investigated. Static pushover analysis was used to evaluate the performance of 4, 8, and 12-story steel frames with seven structural configuration systems. The results showed that the performance of braced frames increased significantly in terms of number of plastic hinges, total base shear and performance point compared to unbraced frames. The capacity curves were maximum in the one-story X-bracing, multi-story X-bracing, and single diagonal bracing systems.

ARTICLE INFO

Article history:

Received 21 April 2022

Revised 17 May 2022

Accepted 9 June 2022

Keywords:

Base shear

Braced steel frames

Capacity design

Performance-based seismic design

Plastic hinge

1. Introduction

Structures designed by seismic code procedures are expected to undergo large deformations in the inelastic range when subjected to strong earthquakes; however, seismic codes are still based on elastic methods. This procedure can cause unpredictable and weak response during strong earthquakes with inelastic activity unevenly distributed among structural elements by Lee et al. (2004). In capacity design, buildings are allowed to be damaged during strong earthquakes. The distribution of this damage is determined by the designer and necessary precautions are taken. In ductile behavior, plastic deformation is adopted in the design. The location and type of these damages are the most important elements of the capacity design and are affected by many factors such as the bracing and the stiffness of the members by Al-Safi et al. (2020). It is known that the stiffness matrix of any structure is given by Eq. (1).

$$[K] = \{F\}\{U\}^{-1} \quad (1)$$

where $\{F\}$ is the external force, $[K]$ the stiffness matrix, and $\{U\}$ denotes the displacements. In other words, the

lower the displacement, the greater the stiffness. Plastic hinge formation distinguishes the location of the building where greater potential damage can occur. In this arrangement, by reaching the maximum number of plastic hinges, theoretically, the building has the highest ultimate load. Otherwise, the building will collapse with less load and less plastic hinges. Achieving the maximum number of plastic hinges could be a new performance goal in seismic design. Higher rigid frames can be obtained by adding bracing systems. Many bracing systems have been proposed in the literature and the most commonly used bracing systems are multistory X-bracing proposed by Aninthaneni and Dhakal (2017), Yang et al. (2019), single diagonal Abou-Elfath et al. (2017), Sabouri-Ghomi and Payandehjoo (2017), Setyowulan et al. (2020), Zeng et al. (2019), V-bracing Kanyilmaz (2017), Salmasi and Sheidaii (2017), one story X-bracing Al-Safi et al. (2021), Jamkhaneh et al. (2019), Mahmoudi et al. (2019), Mashhadiali et al. (2016), concentric braced frames Banihashemi et al. (2015), Cesare et al. (2014), De Stefani et al. (2015), Hammad and Moustafa (2021), Mirjalali et al. (2019), Nezamisavojbolaghi (2020), and K-bracing Tajmir Riahi et al. (2020). In the above literature, there is a lot of research on the braced frames, but

* Corresponding author. E-mail address: i.ameri@eng-su.edu.ye (I. A. Alameri)

most are finite element analysis (FEA) or experimental work with a limited number of stories and limited bracing systems; however, there is no study focus on the performance-based seismic design of these frames with a different bracing system and a different number of stories. This study aims to examine the performance-based seismic design of the most recommended bracing systems in the literature and to find the most effective bracing system for frames out of six bracing systems investigated in terms of plastic hinge number, base shear vs. displacement capacity curve, and performance point. For this purpose, 4, 8, and 12 story steel frames with six bracing configurations (K-bracing, inverted V- bracing, V- bracing, single-diagonal bracing, one story X- bracing, and multi-story X- bracing) were examined.

2. Research Methodology

2.1. Building information

In this study, steel frames with 4, 8 and 12-story were selected to represent low, mid, and high-rise frames. The

frames selected were typically intermediate steel moment frame with $C_d = 3$ and $R = 3.5$. Frames have 4@4 m bays and a story height of 3.2 m. An approximate analysis was carried out to determine the dimensions of element's cross sections. Structural sections of all frames were designed according to AISC 360 (2016) and summarized in Table 1. Earthquake loads were calculated according to IBC (2020) and Class C soil was used. The spectral response acceleration parameters at short period, S_s , and at a period of 1s, S_1 , are 0.36g, 0.17g, respectively. The dead load was accepted as 37 kN/m', live load = 8 kN/m', and finishing load = 6 kN/m'. A36 steel was used. Pushover analysis was performed using Sap2000 Software V22. Six types of bracing systems (Single diagonal, V-bracing, inverted V-bracing, K-bracing, multi-story X-bracing, and one-story X-bracing) compared to the unbraced frame on the number of plastic hinges, base shear vs. displacement capacity curve, and performance point (V, D) (Fig. 1(a-g)). The sections of the columns and beams were kept the same in all frames to investigate the effect of bracing configurations. The connections between beams and columns has been considered to be rigid.

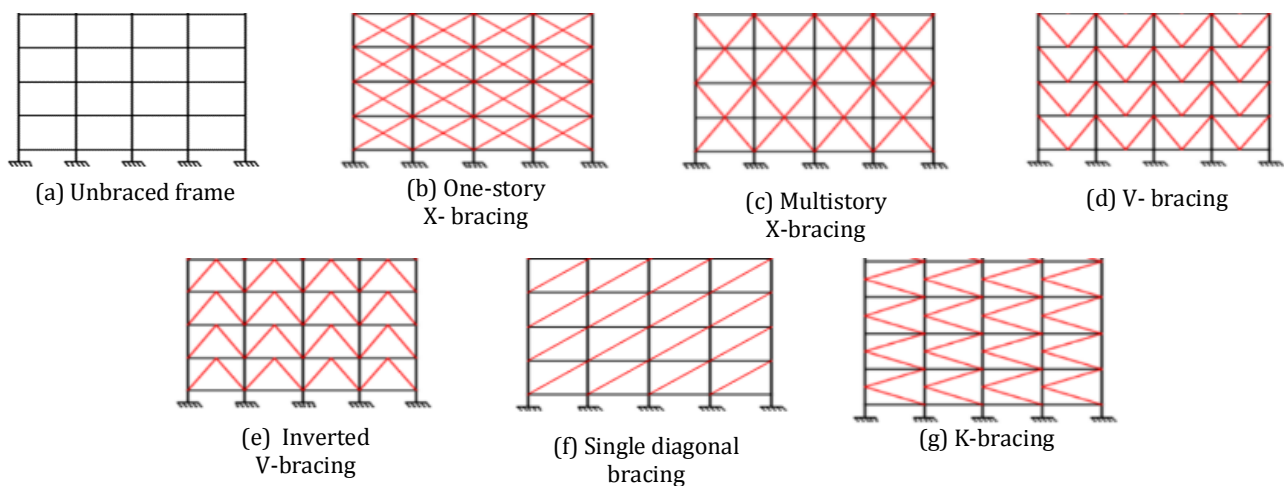


Fig. 1. Types of bracing systems used.

Table 1. Structural sections used in pushover analysis.

Building	Stories	Column	Beam	Bracing
4-story	1 st -4 th	HEB 350	IPE 330	2L 70 × 8 × 0
	1 st -2 nd	HEM 600	IPE 330	2L 70 × 7 × 0
8-story	3 rd -4 th	HEB 550	IPE 330	2L 70 × 7 × 0
	5 th -8 th	HEB 360	IPE 330	2L 50 × 6 × 0
12-story	1 st -2 nd	HEM 700	IPE 330	2L 70 × 8 × 0
	3 rd -4 th	HEM 650	IPE 330	2L70 × 8 × 0
	5 th -8 th	HEB 500	IPE 330	2L60 × 8 × 0
	9 th -12 th	HEB 360	IPE 330	2L60 × 8 × 0

2.2. Plastic hinge properties

The non-linear ($M-\theta$) plastic hinge properties used in the examined frames are shown in Fig. 2. Moment and rotation values are normalized to the corresponding yield values. According to FEMA 356 (2000), the length of the plastic hinge regions is equal to half the section depth.

$$L_p = h/2 \quad (2)$$

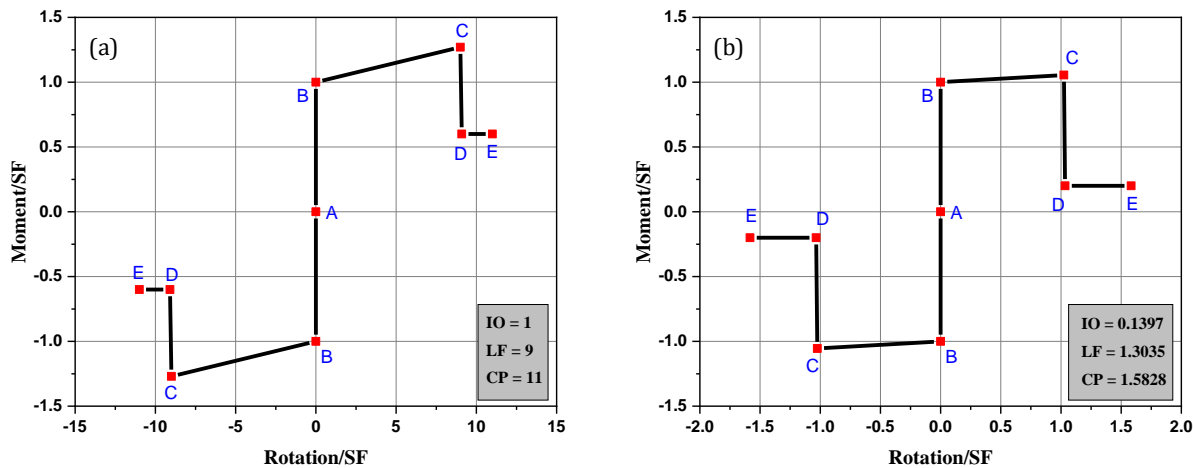


Fig. 2. Plastic hinge properties for (a) beams, and (b) columns.

Table 2. Deformation limits by Naeim (2001).

Performance limit				
Interstory drift limit	Immediate occupancy	Damage control	Life safety	Structural stability
Maximum total drift	0.01	0.01-0.002	0.02	0.03 V_i/P_i

3. Results and Discussion

3.1. Plastic hinge formation

In this study, beam and column sections were kept the same in all configurations for comparison. The plastic hinges formed in the structural members (columns and beams) of braced and unbraced frames are shown in Figs. 3-5 and summarized in Tables 3-5. The performance of plastic hinges is classified into three levels as follows proposed by FEMA 356:

- “Immediate Occupancy (IO): Damage is light, and structure retains most of its original strength and stiffness. There may be minor cracking on the structural members”.
- “Life Safety (LS): Substantial damage to the structure and the structure may have lost a large portion of its strength and stiffness”.
- “Collapse Prevention (CP): Severe damage and little strength and stiffness remains. Building is unstable and is near collapse”.

In the 8- and 12-story buildings, the number of plastic hinges formed was higher in all braced frames compared to the unbraced frame. On the other hand, in low rise (4-

where L_p is the length of plastic hinge, and h is the depth of the section.

Depending on the performance level chosen, a constant lateral drift should be applied at the top node of all frames. Lateral drift limits must meet the limits given in Table 2 (Naeim 2001). Assuming life safety performance level, lateral drift was calculated as 0.02 of the frame height, and base shear remained variable.

story) frames, the number of plastic hinges increased in some bracing systems, while it decreased in others. Fig. 3 and Table 3 show that the maximum number of plastic hinges formed in 4-story frames are in V-bracing and then in inverted V-bracing. In this system, the performance levels remained “Life safety” as assumed, but the other systems were moved to the “Collapse prevention” performance level. Compared to the unbraced frame, the number of plastic hinges increased by 45% and 19% for V-bracing, inverted V-bracing systems, respectively.

In the mid-height frames (8-story), Fig. 4 and Table 4 show that, plastic hinges increased in all braced frames and the maximum number of plastic hinges was noticed in the inverted V-bracing system. The number of plastic hinges compared to the unbraced frame were increased by 32, 28, 22, 20, 20, and 18% for the inverted V-bracing, multistory X-bracing, V-bracing, one-story X-bracing, single diagonal bracing, and K-bracing, respectively. In addition, the final performance level of inverted V-bracing, V-bracing, and K-bracing remained life safety (LS) performance level; however, other bracing systems have moved to the collapse prevention (CP) performance level. This is the main reason for the increase seen in the capacity curves of these frames.

In the high-rise building, Fig. 5 and Table 5 show that, the behavior was similar to that of mid-rise buildings. All frames with bracing showed an increase in the number of plastic hinges compared to the unbraced frame. Moreover, single diagonal, multistory X-bracing, one-story X-bracing, and K-bracing were moved to the performance level of collapse prevention (CP), while other systems remained at the life safety (LS) performance level. Compared to the unbraced frame, the K-bracing, multistory

X-bracing, single diagonal, one story X-bracing, V-bracing, and inverted V-bracing systems showed an increase

in the number of plastic hinges by 26, 25, 17, 12, 12, and 12%, respectively.

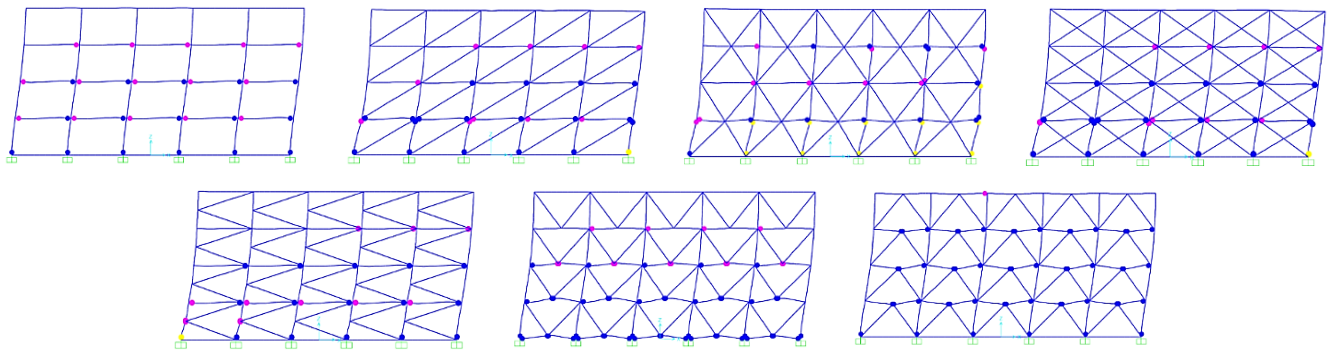


Fig. 3. Hinge severity legend for 4-story buildings.

Table 3. Final performance level calculations for 4-story buildings.

System type	Element	Total number of hinges	<10 (%)	<LS (%)	<CP (%)	>CP (%)	Performance level
Unbraced frame	Beam	25	60	40	0	0	LS
	Column	6	0	100	0	0	
Single diagonal bracing	Beam	19	42	58	0	0	CP
	Column	6	0	83	0	17	
Multistory-X bracing	Beam	16	38	63	0	0	CP
	Column	18	22	17	0	61	
One-story X-bracing	Beam	19	37	63	0	0	CP
	Column	9	11	78	0	11	
K-bracing	Beam	18	44	56	0	0	CP
	Column	8	25	63	0	13	
V-bracing	beam	39	23	77	0	0	LS
	column	6	0	100	0	0	
Inverted V-bracing	beam	31	3	97	0	0	LS
	column	6	0	100	0	0	

Table 4. Final performance level calculations for 8-story buildings.

System type	Element	Total number of hinges	<10 (%)	<LS (%)	<CP (%)	>CP (%)	Performance level
Unbraced frame	Beam	50	40	60	0	0	LS
	Column	0.0	0	0	0	0	
Single diagonal bracing	Beam	54	39	61	0	0	CP
	Column	6	0	83	0	17	
Multistory-X bracing	Beam	52	37	63	0	0	CP
	Column	12	0	83	0	17	
One-story X-bracing	Beam	54	37	63	0	0	CP
	Column	6	0	83	0	17	
K-bracing	Beam	53	34	66	0	0	LS
	Column	6	0	100	0	0	
V-bracing	beam	55	18	82	0	0	LS
	column	6	0	100	0	0	
Inverted V-bracing	beam	60	18	82	0	0	LS
	column	6	83	17	0	0	

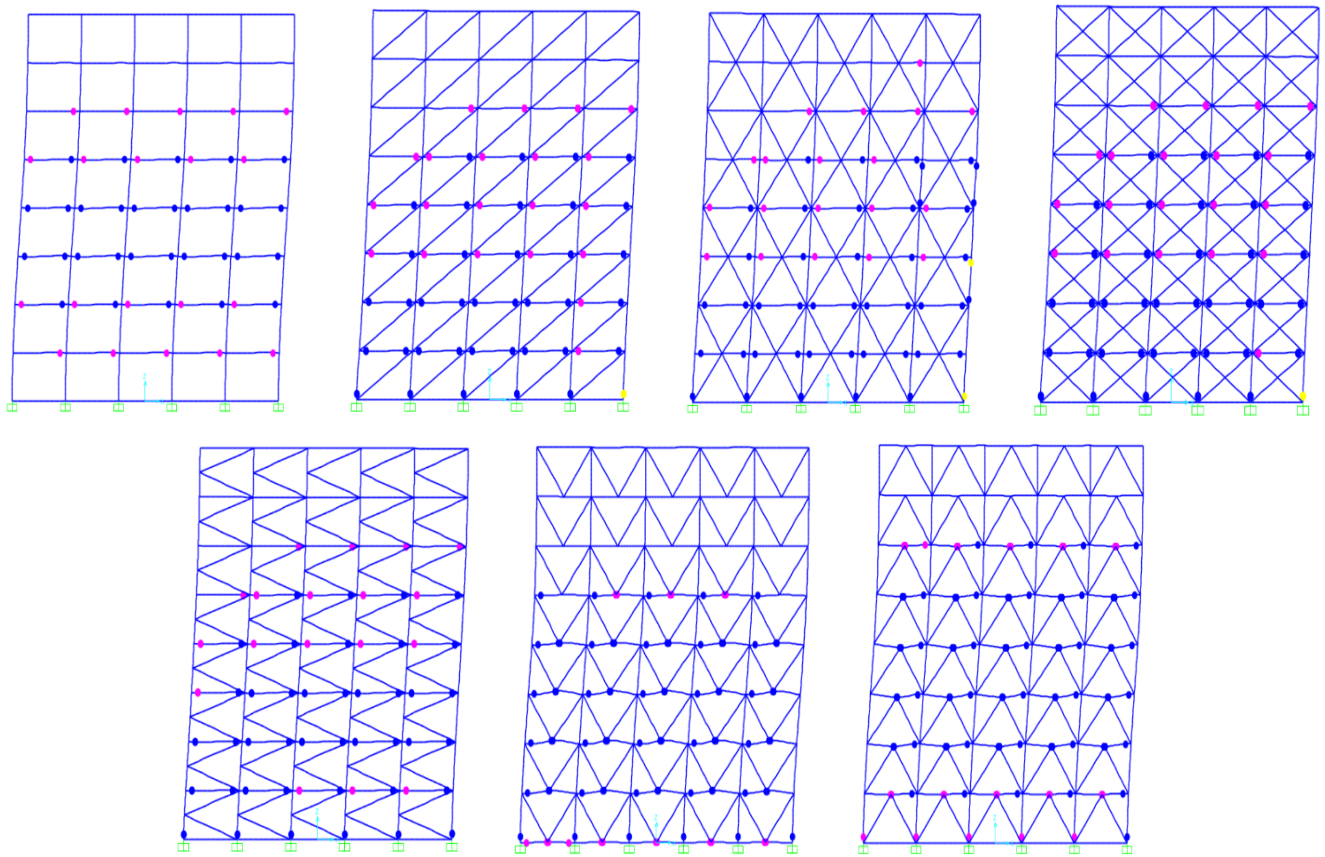


Fig. 4. Hinge severity legend for 8-story buildings.

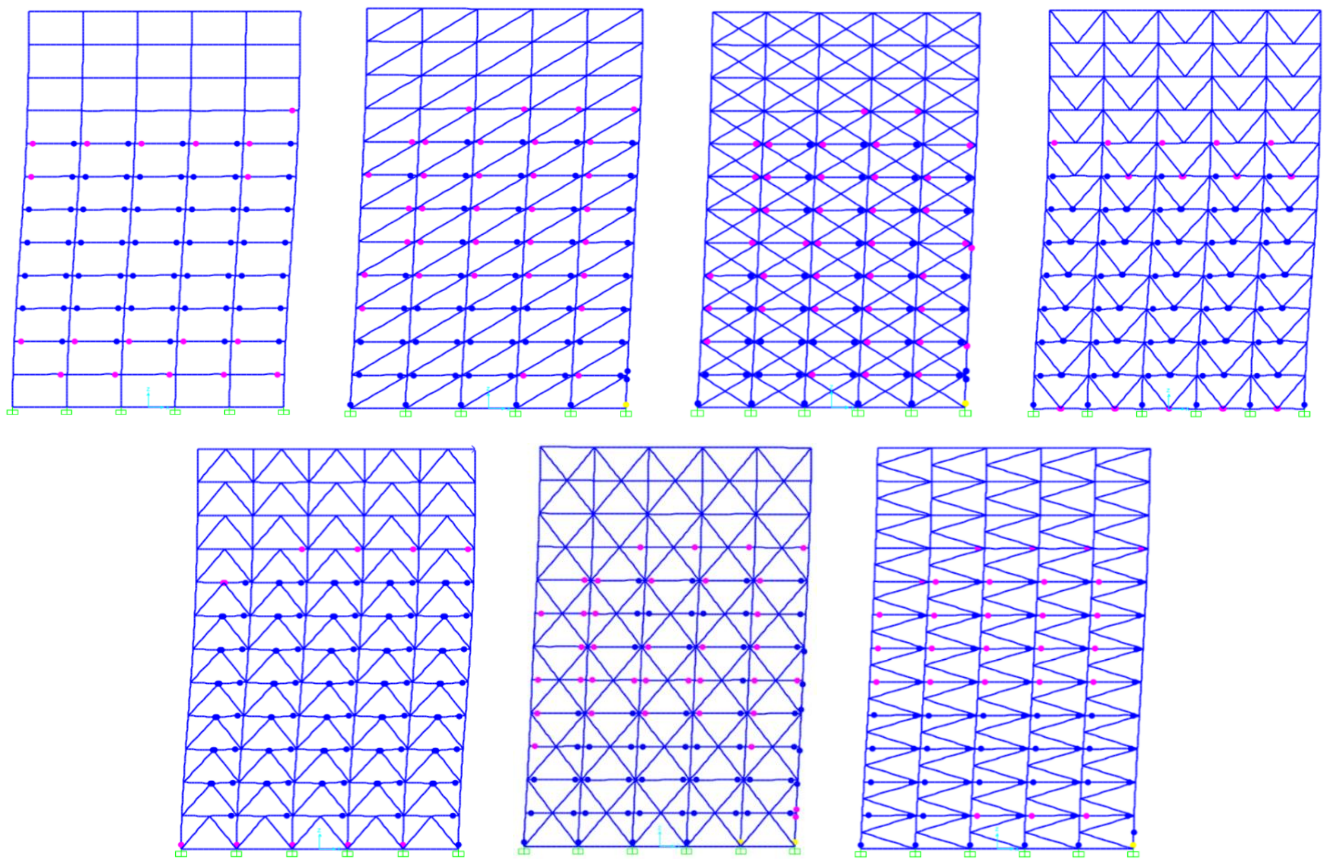


Fig. 5. Hinge severity legend for 12-story buildings.

Table 5. Final performance level calculations for 12-story buildings.

System type	Element	Total number of hinges	<IO (%)	<LS (%)	<CP (%)	>CP (%)	Performance level
Unbraced frame	Beam	76	24	76	0	0	LS
	Column	0	0	0	0	0	
Single diagonal bracing	Beam	82	40	60	0	0	CP
	Column	7	0	86	0	14	
Multistory-X bracing	Beam	82	41	59	0	0	CP
	Column	13	15	69	0	15	
One-story X-bracing	Beam	76	50	50	0	0	CP
	Column	9	22	67	0	11	
K-bracing	Beam	89	30	70	0	0	CP
	Column	7	0	86	0	14	
V-bracing	beam	79	18	82	0	0	LS
	column	6	0	100	0	0	
Inverted V-bracing	beam	79	6	94	0	0	LS
	column	6	83	17	0	0	

3.2. Capacity curves and performance point results

Static pushover analysis was performed to calculate the base shear vs. displacement capacity curves of all studied frames (Fig. 6). As mentioned in the previous section, the capacity curve is directly proportional to the number of plastic hinges forms. Fig. 6 clearly shows that the capacity curves of braced frames significantly increased. In low rise frames (Fig. 6a) single diagonal and one-story X-bracing systems showed the highest base shear values. In the single diagonal bracing, one-story X-bracing, multistorey X-bracing, K-bracing, V-bracing, and inverted V-bracing base shear was increased by 823, 820, 667, 221,107, and 59% in comparison to the unbraced frame. The reason for this increase is the transition of single diagonal, multistory X bracing, one-story X bracing and K bracing systems from LS performance level to CP performance level. Hence, the total plastic moment carried by these hinges increased; however, for the other systems the number of plastic hinges increased but the performance level remained the same. The capacity curves of the mid-rise (8-story) frames are shown in Fig. 6b and the maximum base shear value is observed in the multi-story X bracing system. Similar to low-rise

frames this significant increase was because the performance level of these frames changed from LS into CP. The increase in base shear compared to the unbraced system was 502, 494, 492, 202, 97, and 64% for multistory X-bracing, one-story X-bracing, single diagonal, K-bracing, V-bracing, and inverted V-bracing systems. In high-rise (12-story) frames, base shear value was maximum in the one-story X-bracing system followed by the multistory X-bracing and single diagonal systems (Fig. 6c). In comparison with the unbraced frame, total base shear was increased by 517, 484, 481, 208, 103, and 68% for one story X-bracing, multistory X-bracing, single diagonal bracing, K-bracing, V-bracing, and inverted V-bracing systems, respectively.

In this study, the performance point was evaluated according to the FEMA 440 Displacement Modification, FEMA 356 Coefficient Method, FEMA 440 Equivalent Linearization and ATC-40 Capacity Spectrum methods (Tables 6-8). The results show that the performance point of the bracing systems increases the base shear value corresponding to a decrease in the roof displacement. This showed that the stiffness of the braced frame was greater than that of the unbraced frame. Thus, the number of plastic hinges and capacity curves also increased.

Table 6. Performance point results for 4-story buildings.

System type	ACT-40 Capacity spectrum		FEMA356 Coefficient method		FEMA440 Equivalent linearization		FEMA440 Displacement modification	
	V (kN)	D (mm)	V (kN)	D (mm)	V (kN)	D (mm)	V (kN)	D(mm)
Unbraced frame	712.74	42.92	1155.25	69.67	712.75	42.92	1377.87	83.13
Single diagonal bracing	1038.39	9.63	2214.59	19.70	1057.90	9.80	2040.33	18.21
Multistory X-bracing	1045.24	11.89	2056.07	22.79	1045.25	11.89	1698.78	19.18
One-story X-bracing	1042.78	9.67	2155.73	19.20	1054.99	9.78	1961.03	17.53
K-bracing	1003.15	21.19	1715.43	36.19	1005.52	21.24	1660.71	35.04
V-bracing	1055.99	14.87	1698.36	28.03	1055.99	14.87	1544.01	24.67
Inverted V-bracing	1001.64	32.48	2413.19	68.18	1470.15	42.52	1517.24	43.52

Table 7. Performance point results for 8-story buildings.

System type	ACT-40 Capacity spectrum		FEMA356 Coefficient method		FEMA440 Equivalent linearization		FEMA440 Displacement modification	
	V (kN)	D (mm)	V (kN)	D (mm)	V (kN)	D (mm)	V (kN)	D(mm)
Unbraced frame	805.30	84.81	1204.33	127.09	805.30	84.81	1204.33	127.09
Single diagonal bracing	1721.64	41.39	2766.90	65.43	1756.43	42.19	2929.68	69.17
Multistory X-bracing	1702.77	42.18	2599.38	63.16	1702.77	42.17	2656.81	64.45
One-story X-bracing	1709.22	41.07	2172.38	51.72	1722.99	41.51	2798.64	66.10
K-bracing	1284.75	55.42	1908.70	82.16	1285.39	55.45	1949.70	83.92
V-bracing	1486.54	47.13	2111.51	71.66	1486.54	47.14	2137.28	72.69
Inverted V-bracing	1159.96	67.10	2537.95	125.76	1574.99	84.95	2537.95	125.76

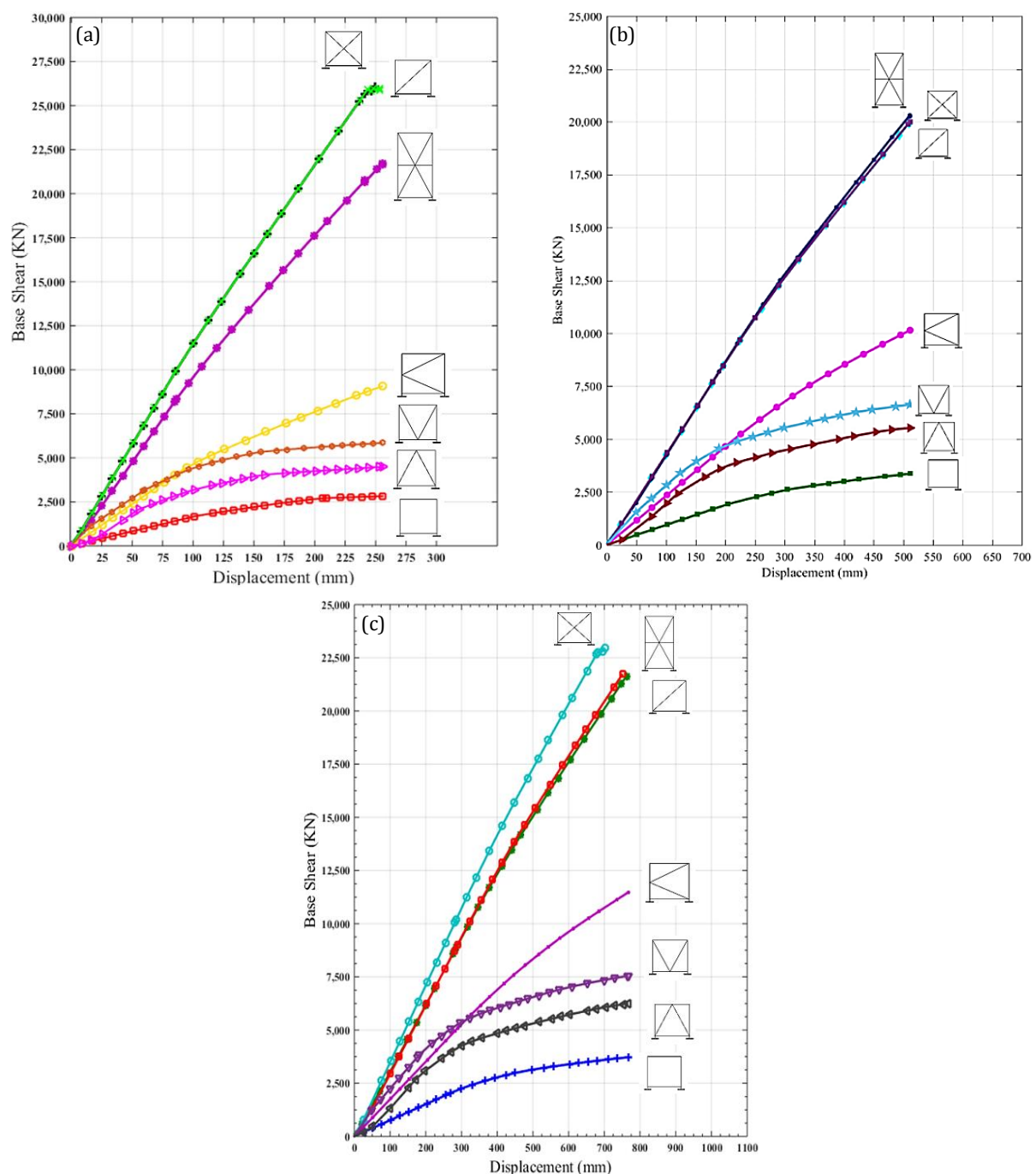
**Fig. 6.** Base shear vs. displacement capacity curves for (a) 4-story, (b) 8-story, and (c) 12-story buildings.

Table 8. Performance point results for 12-story buildings.

System type	ACT-40 Capacity spectrum		FEMA356 Coefficient method		FEMA440 Equivalent linearization		FEMA440 Displacement modification	
	V (kN)	D (mm)	V (kN)	D (mm)	V (kN)	D (mm)	V (kN)	D (mm)
Unbraced frame	734.98	121.04	1181.57	194.94	734.99	121.04	1181.57	194.94
Single diagonal bracing	1441.73	60.79	2860.02	117.30	1603.81	97.33	2860.02	117.30
Multistory X-bracing	1434.92	64.56	2550.19	107.87	1461.74	65.62	2250.19	107.87
One-story X-bracing	1595.66	59.07	2809.42	101.04	1680.15	61.99	2809.42	101.04
K-bracing	1120.08	80.29	1873.74	133.61	1145.37	82.08	1873.74	133.61
V-bracing	1242.75	64.81	1947.55	109.69	1283.65	67.37	1947.55	109.69
Inverted V-bracing	982.08	95.03	2452.69	197.05	1413.12	123.83	2452.69	197.05

4. Conclusions

In this study, a total of six bracing configurations were investigated based on the number of plastic hinges formed, the capacity curve and performance points. The following conclusions can be drawn from the study:

- Bracing members are important to resist lateral loads and, in this study, all braced frames showed a higher base shear as well as a greater number of plastic hinges compared to the unbraced frame.
- Multi-story X-bracing, one-story X-bracing, and single diagonal bracing systems have the highest capacity. Thus, the increase in the base shear for the 4-story, 8-story, and 12-story frames was 823%, 502%, and 517%, respectively.
- According to the FEMA 440 displacement modification, FEMA 356 coefficient method, FEMA 440 equivalent linearization, and ATC-40 capacity spectrum methods, the performance point of the bracing systems has a large base shear corresponding to a small roof displacement. This indicates that the rigidity of the braced frame is greater than the unbraced frame.

For future studies, performance-based design can be investigated on different joint types or different support types.

Acknowledgements

None declared.

Funding

The authors received no financial support for the research, authorship, and/or publication of this manuscript.

Conflict of Interest

The authors declared no potential conflicts of interest with respect to the research, authorship, and/or publication of this manuscript.

REFERENCES

- Abou-Elfath H, Ramadan M, Alkanai F (2017). Upgrading the seismic capacity of existing RC buildings using buckling restrained braces. *Alexandria Engineering Journal*, 56(2), 251–262.
- AISC 360 (2016). Specification for Structural Steel Buildings. *American Institute of Steel Construction*.
- Al-Safi S, Alameri IA, Badhib RAM, Kuleib M (2020). Evaluation of performance-based earthquake engineering in Yemen. *Challenge Journal of Structural Mechanics*, 6(1), 10–22.
- Al-Safi S, Alameri I, Wasel WA, Al-kadasi AB (2021). Linear and nonlinear behavior of steel buildings with different bracing systems. *International Journal of Steel Structures*, 21(2), 475–486.
- Aninthaneni PK, Dhakal RP (2017). Prediction of lateral stiffness and fundamental period of concentrically braced frame buildings. *Bulletin of Earthquake Engineering*, 15(7), 3053–3082.
- Banihashemi MR, Mirzagoltabar AR, Tavakoli HR (2015). Performance-based plastic design method for steel concentric braced frames. *International Journal of Advanced Structural Engineering*, 7(3), 281–293.
- Cesare AD, Ponzo FC, Nigro D (2014). Assessment of the performance of hysteretic energy dissipation bracing systems. *Bulletin of Earthquake Engineering*, 12(6), 2777–2796.
- De Stefani L, Scotta R, Lazzari M (2015). Optimal design of seismic retrofitting of RC frames with eccentric steel bracing. *Bulletin of Earthquake Engineering*, 13(2), 613–633.
- Hammad A, Moustafa MA (2021). Numerical analysis of special concentric braced frames using experimentally-validated fatigue and fracture model under short and long duration earthquakes. *Bulletin of Earthquake Engineering*, 19(1), 287–316.
- IBC (2020). International Building Code. International Code Council.
- Jamkhaneh ME, Ebrahimi AH, Amiri MS (2019). Investigation of the seismic behavior of brace frames with new corrugated all-steel buckling restrained brace. *International Journal of Steel Structures*, 19(4), 1225–1236.
- Kanyilmaz A (2017). Secondary frame action in concentrically braced frames designed for moderate seismicity: A full scale experimental study. *Bulletin of Earthquake Engineering*, 15(5), 2101–2127.
- Lee SS, Goel SC, Chao SH (2004). Performance-based seismic design of steel moment frames using target drift and yield mechanism. *13th World Conference on Earthquake Engineering*, Vancouver, BC, Canada.
- Mahmoudi M, Shirpour A, Zarezadeh A (2019). The effects of mid-span connection specifications on compressive performance of cross (X) braces. *International Journal of Steel Structures*, 19(4), 1125–1133.
- Mashhadiali N, Gholhaki M, Kheyroddin A, Zahiri-Hashemi R (2016). Technical note: Analytical evaluation of the vulnerability of framed tall buildings with steel plate shear wall to progressive collapse. *International Journal of Civil Engineering*, 14(8), 595–608.
- Mirjalali H, Ghasemi M, Labbafzadeh MS (2019). Effect of bracing type and topology on progressive collapse resistance of eccentrically

- braced frames. *International Journal of Steel Structures*, 19(5), 1497–1510.
- Naeim F (2001). *The Seismic Design Handbook* (2nd ed.). Springer US.
- Nezamisavojbolaghi K (2020). Using concentric and zipper steel braces by comparison of effect on improved seismic performance level of concrete moment frame structures with moderate ductility. *SN Applied Sciences*, 2(1), 1–7.
- Sabouri-Ghomi S, Payandehjoo B (2017). Analytical and experimental studies of the seismic performance of drawer bracing system (DBS). *International Journal of Civil Engineering*, 15(8), 1087–1096.
- Salmasi AC, Sheidaii MR (2017). Assessment of eccentrically braced frames strength against progressive collapse. *International Journal of Steel Structures*, 17(2), 543–551.
- Setyowulan D, Susanti L, Wijaya MN (2020). Study on the behavior of a one way eccentric braced frame under lateral load. *Asian Journal of Civil Engineering*, 21(4), 733–739.
- Tajmir Riahi H, Zeynalian M, Rabiei A, Ferdosi E (2020). Seismic collapse assessment of K-shaped bracings in cold-formed steel frames. *Structures*, 25, 256–267.
- Yang TY, Sheikh H, Tobber L (2019). Influence of the brace configurations on the seismic performance of steel concentrically braced frames. *Frontiers in Built Environment*, 5.
- Zeng L, Zhang W, Ding Y (2019). Representative strain-based fatigue and fracture evaluation of I-shaped steel bracing members using the fiber model. *Journal of Constructional Steel Research*, 160, 476–489.



Research Article

Effect of waste steel tire wired concrete on the mechanical behavior under impact loading

Hasan Selim Şengel ^{a,*} , Kutluhan Ethem Kınık ^a , Hakan Erol ^a , Mehmet Canbaz ^a 

^a Department of Civil Engineering, Eskişehir Osmangazi University, 26480 Eskişehir, Türkiye

ABSTRACT

In this experimental study the effect of waste steel tire wire was investigated on the concrete bollards of mechanical behavior under impact loading. Concrete bollards were produced using three different dimensions with three different volumes of waste steel tire wire (0%, 5% and 10%). The concrete was 30 MPa strength. The concrete bollards were cast into molds with a size of 100x100 mm, 150x150 mm and 200x200 mm and standard length of 1100 mm prism. Nine cube specimens of three different dimensions are tested. 84 kg of an impact load is used with the drop height of 400 mm in this study. Compressive strength tests were achieved. Concrete bollards were kept in laboratory standard conditions. According to the results of study compressive strength of the concrete vary between 25-30 MPa. The use of waste steel tire wire in the concrete bollards contributes to the less crack, less deflection, more acceleration and more energy dissipation at the end of the specimens. The experimental test aimed to research the effect of waste steel tire wired concrete on the mechanical behavior under impact loading as a possible environmentally friendly and sustainable solution. It can be said that the results provide the potential usage of waste steel tire wire manufacturing friendly to nature and sustainability of the concrete bollards. Generally, the usage of waste steel tire wire in concrete could be an innovative method in the construction industry.

ARTICLE INFO

Article history:

Received 27 May 2022

Revised 24 June 2022

Accepted 13 July 2022

Keywords:

Sustainability

Concrete bollards

Steel fiber

Recycled tire

Impact load

Waste steel tire wire

1. Introduction

Rapid technological developments, industrialization and population growth made the humankind face to face with problems that have not encountered before, very quickly. The increment in the amount of waste product is one of the important consequences of this. With the increment in the amount number of wastes, the rapid pollution of nature and the environment threatens bios in terms of health. For this reason, researches on recycling of wastes are intensively carried out and implemented. Significant achievements can be acquired by recycling waste tires that have reached the end of span. Protecting the nature and keeping it clean is the most important achievement. The product with high added value obtained by recycling can be used as a raw material in the production of different products. With the decrease in

imports, it can be beneficial to close the current account deficit and to employment by creating a new business branch.

It is the main duty of humankind to leave a cleaner, more sustainable environment and nature to posterity. Developed countries constitute millions of waste tires every year in consequence of the rapid enhancement of vehicles. Approximately 1.4 billion tires are sold out globally every year and accordingly many of them fall into decay and became waste. These tires waste generate one of the most important problems of waste, as it is large in volume and because of their durability (Lo Presti 2013). By recycling waste tires, rubber and steel wire can be obtained.

Concrete which has low tensile strength but on the contrary, high compressive strength is a well-known building material. In order to improve these properties,

* Corresponding author. Tel.: +90-222-239-3750 ; Fax: +90-222-229-0535 ; E-mail address: ssengel@ogu.edu.tr (H. S. Şengel)

lots of researches have been done and new components have been developed. The most common is fiber-reinforced concrete. The idea of using fibers is to increase the tensile strength of concrete by enhancing the load bearing capacity by bridging cracks. It has been proved that the usage of steel fibers controls the crack attitude and changes it to ductile (Faghih 2017). The main purposes of modern engineers by adding fiber to concrete can be written as to improve the plastic crack properties of fresh concrete, tensile and flexural strengths, impact strength and toughness, and durability of concrete. It is also to control the failure mode and crack formation with post-crack ductility (Hannat 2003). Recently, many researches about the usage of rubber and steel wires recycled from waste tires in concrete have been done. It has been proven that the concrete acquired by adding waste steel tire wires has acceptable improvements especially in toughness and post-crack behavior. Consequently, waste steel tire wired concrete seems to be a promising candidate for both structural and non-structural executions (Aiello et al. 2009).

Zeynal (2008) conducted an experimental study to investigate the effect of steel fiber and water/cement ratios on the impact strength and mechanical properties of steel fiber concrete. With the usage of only 0.4%, 0.8% and 1.2% long steel fibers by volume in concrete; it can be increased by 2% to 10% in compressive strength, 13% to 42% in split tensile strength, and 14% to 115% in flexural strength. He concluded that an increase in the value of impact number that causes fragile ranging from 3.5 to 23.9 times to be obtained. Şengül (2016) researched to examine the mechanical properties of concrete containing steel wires obtained from waste tires. Concrete was produced by using different ratios of steel fibers obtained from waste tires with an average diameter of 0.3, 0.6, 1.4 mm and an average length of 5 cm. It was observed that the splitting tensile strength slightly increased as the steel wire content increased. The use of steel wires obtained from waste tires in concrete did not significantly affect the compressive, flexural and splitting tensile strength of the concrete. Concrete containing steel wires recovered from waste tires show the similar behavior in the descending part of the load-deflection curves that is of residual strength and toughness, compared to concrete containing standard steel fibers acquired in bending. Test results showed that steel wires recycled from waste tires can be used in concrete instead of standard steel fibers. Senesavath's (2021) experimental study investigated the effect of steel wires recycled waste tire on concrete properties. By using the waste steel tire wire, a more ductile behavior was obtained after the first crack formation and an increase in energy absorption capacity was observed. Flexural toughness showed an increasing trend with the addition of waste tire steel wire. Siraj (2009) investigated the mechanical behavior of steel wire obtained from waste tires in concrete. The experimental study used 0.5, 1.0 and 1.5% waste steel tire wire by volume. The test specimens were produced in the dimensions of 150 mm cube specimen, 150 mm diameter with 63.5 mm height cylindrical specimen and 100x100x500 mm beam. With the addition of steel wire recycled waste tire, enormous in-

creases in the flexural strength and post-crack energy absorption capacity of concrete were achieved. In addition, it was observed that the first crack and final failure impact strength increased significantly in the repeated drop weight test. Mastali (2018) conducted a study in which the properties of steel wire recycled waste tire concrete were determined. In the experimental study, samples with varying fiber content by volume (0.5, 0.75, 1.0, and 1.5) were produced. When examining the first crack and the final crack resistance depending on the waste steel tire wire usage, the impact resistance increases by creating bridging. In addition it is stated that waste steel tire wire gives the superlative productivity when compared to industrial steel fibers in terms of the optimum mechanical properties, impact resistance and minimum cost. And also Mastalli (2019) conducted another study on high-strength concrete in which the effects of steel wire recycled waste tire were compared. The experimental study has a miscellaneous comparison that as the volume of waste steel tire wire increases, the initial impact resistance, the final impact resistance, the drop weight number after crack initiation until failure, the deformation ability, the energy absorption capacity, and the impact energy increase.

The data obtained from the experimental study on the effect of waste tire steel wire by recycling waste tires under impact loading of concrete are examined in this article. There are lots of studies about industrial steel fiber or steel wire recovered from waste tire on concrete, but a few about impact loading or blasting. In this research paper on concrete bollards that are often faced to impact loading, differently from other researches, waste steel tire wire is added for the purpose of examine impact loading.

2. Experimental Study

A total of 9 square based prismatic concrete specimens, with and without waste steel tire wire were designed for impact load. The specimens represent a prototype of concrete bollards that help guide traffic flow of vehicular. These concrete bollards are characterized by low to moderate waste steel tire wire by ratio and cross section. Geometry and waste steel tire wire ratio details of the specimens indicated in Table 1. All the specimens had 1100 mm height. The columns were divided into three sets. All sets had three specimens. Each set had a square cross section of 100 mm, 150 mm and 200 mm by respectively. All the collected data were achieved with the help of LabView SignalExpress program by National Instruments during the experimental study. Also all the collected data processed with the help of DIAdem program by National Instruments.

2.1. Materials

Three types of concrete mix with waste steel tire wire were used with volume ratio of 0%, 5% and 10% for the concrete bollards. The steel wire was obtained from waste tire is shown in Fig. 1. The waste steel tire wire were added to the concrete mixing machine by desired

volume ratio and waited three minutes for an adequate mixture in each time. Then by sufficient time for curing and gaining strength, all the testing of specimens was completed in 7 days. Two piece of 150 mm test cubes were used to obtain the cube strength of concrete for specimens and the mean strength was recorded 30 MPa. The cubes were tested at the age of 28 days, at the same time first specimen was tested in the laboratory. Because of understanding the effect of steel wire recovered waste tire, three concrete mix (0%, 5% and 10%) used for concrete bollards.

2.2. Method

A total of 9 square based prismatic specimens were casted using appropriate moulds and prepared at the same time. The columns were divided into three sets. All sets had the ratio of the area of longitudinal steel bar to the area of the specimen same as 0.5%. The concrete cover was provided in all the columns 8 mm. The concrete thickness of about 50 mm was cast between ends of the longitudinal bars on both the top and bottom surfaces of the specimens. The specimens cured in the la-

boratory conditions. Three different types of specimens for tests were casted in 100x100 mm, 150x150 mm and 200x200 mm cross section area and the length of 1100 mm were produced. The casting and concreting of the concrete bollards are shown in Fig. 2. Three different cross section and three volume of waste steel wire, nine specimens were produced.



Fig. 1. Waste steel tire wire sample used for tests.



Fig. 2. Appearance of the concrete bollards while casting and concrete working.

Table 1. Properties of the test specimens.

Specimen	Cross-section (mm ²)	Length (mm)	Waste steel ratio (%)
C10x10-0S	100x100	1100	0
C10x10-5S	100x100	1100	5
C10x10-10S	100x100	1100	10
C15x15-0S	150x150	1100	0
C15x15-5S	150x150	1100	5
C15x15-10S	150x150	1100	10
C20x20-0S	200x200	1100	0
C20x20-5S	200x200	1100	5
C20x20-10S	200x200	1100	10

The experimental setups of impact loading with the drop weight machine are shown in Fig. 3. The experimental setup of drop weight machine was manufactured to research the impact loading test of specimens. After the amount of load determined for the experimental study is adjusted, the load hits the determined area of the

sample by making a free fall motion on a rail. This study uses an impact load of 84 kg with the drop height of 400 mm. The accelerometers, LVDTs and load cell are also shown in Fig. 3. With the specially designed supports for the concrete bollard sample, it is ensured that the element act as cantilever for this experimental test.



Fig. 3. Set-up for the impact loading test.

3. Results and Discussion

3.1. Displacement – time graphs assessment

The displacement time graphs of the concrete bollards were acquired from the LVDTs at the right and left end sides of the specimen. The maximum deformations of the concrete bollards under impact loading were obtained 60.72 mm, 59.10 mm and 57.10 mm for 100x100 mm cross section of the specimens. Similarly, 22.83 mm, 22.30 mm and 19.80 mm for the 150x150 mm cross section specimens and 10.80 mm, 10.50 mm and 9.20 mm for the 200x200 mm cross section specimens (by respectively %0, %5 and %10 waste steel tire wire ratio). The maximum deformation of the concrete bollards under impact loading decreased by 6% to 15% depends on the waste steel tire wire content by volume. And also, the maximum deformation of the concrete bollards under impact loading increased depends on the cross section decreased. The experimentally obtained maximum deformations at the end of the concrete bollards versus steel ratio are given in Fig. 4. Maximum deformations of cross section 200x200 mm concrete bollards are very small and these are mostly elastic deformations and a

low part of it is plastic. However while the cross section of the concrete bollards under impact load decreased, deformations are ascended which mostly plastic deformations and a low part of it is elastic.

The residual deformations of the concrete bollards under impact loading were obtained 54.15 mm, 51.69 mm and 48.66 mm for 100x100 mm cross section of the specimens. Similarly, 14.11 mm, 13.27 mm and 11.80 mm for the 150x150 mm cross section specimens and 1.23 mm, 1.13 mm and 0.92 mm for the 200x200 mm cross section specimens (by respectively %0, %5 and %10 waste steel tire wire ratio). The residual deformation of the concrete bollards under impact loading decreased by 10% to 25% depends on the waste steel tire wire content by volume. And also, the residual deformation of the concrete bollards under impact loading increased depends on the cross section decreased. The experimentally obtained residual deformations at the end of the concrete bollards versus steel ratio are given in Fig. 5.

According to these results, the maximum deformation of concrete bollards decreases as the waste steel tire wire ratio increases. Thus, as their capacity increases, they have more ability of deformation. They have a greater impact load carrying capacity.

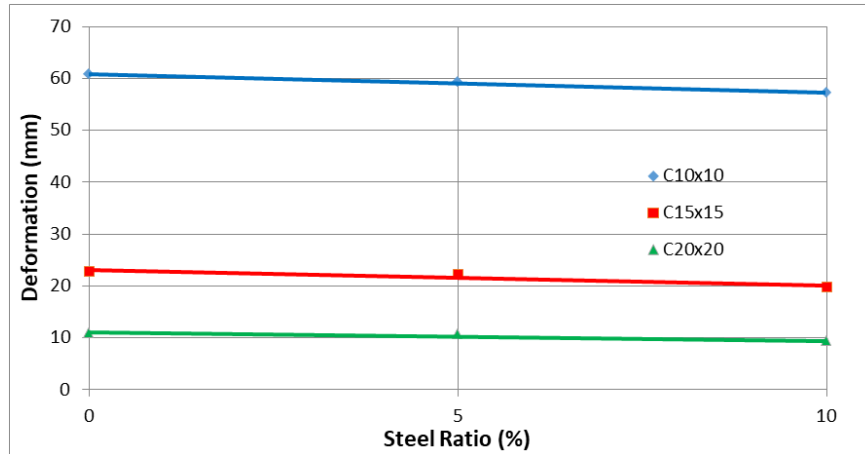


Fig. 4. Maximum deformation – steel ratio relationship obtained experimentally under impact loading.

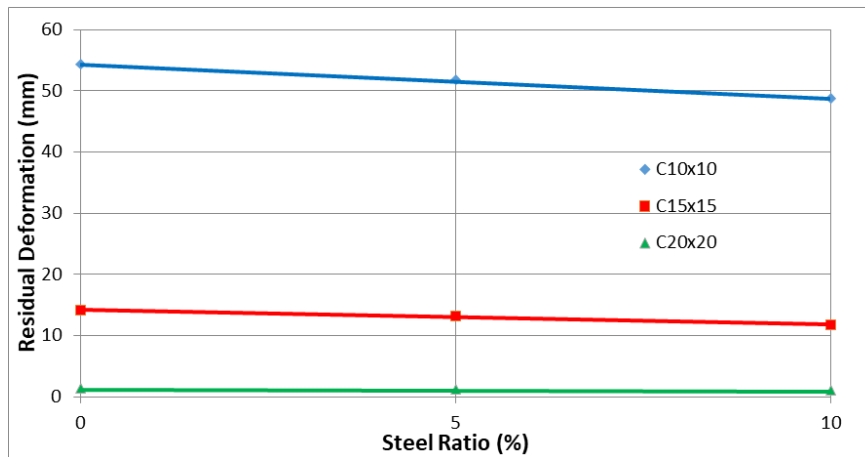


Fig. 5. Residual deformation – steel ratio relationship obtained experimentally under impact loading.

Displacement - time graphs of the concrete bollards according to waste steel tire wire ratio for all sections separately are given in Fig. 6. And also for all sections displacement versus time graphs are given below in Fig. 7.

3.2. Acceleration – time graphs assessment

The acceleration time graphs of the concrete bollards were acquired from the accelerometers at the right and left mid sides of the specimen. The maximum acceleration of the concrete bollards under impact loading were obtained 53.3, 59.6 and 64.9 g for 100x100 mm cross

section of the specimens. Similarly, 81.6, 87.0 and 93.9 g for the 150x150 mm cross section specimens and 98.5, 106.2 and 113.1 mm for the 200x200 mm cross section specimens (by respectively 0%, 5% and 10% waste steel tire wire ratio). The maximum acceleration of the concrete bollards under impact loading increased by 6% to 17% depends on the waste steel tire wire content by volume. And also, the maximum acceleration of the concrete bollards under impact loading increased depends on the cross section increased. The experimentally obtained maximum accelerations at the end of the concrete bollards versus steel ratio are given in Fig. 8.

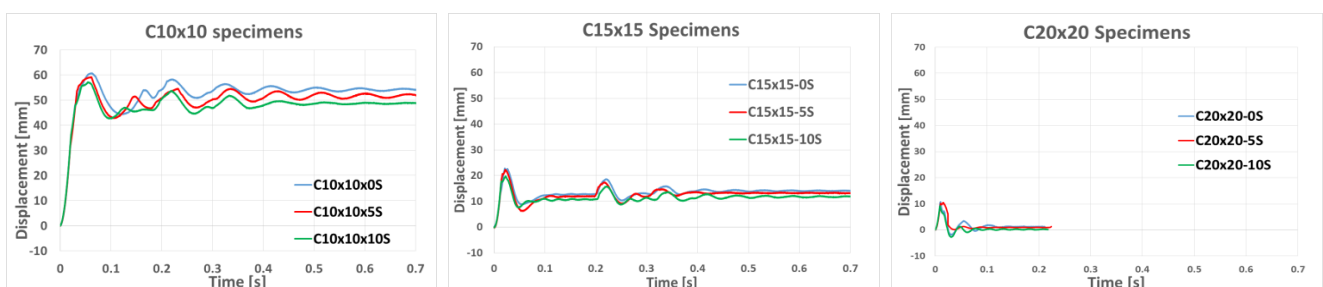


Fig. 6. Displacement – time graphs of the concrete bollards under impact loading.

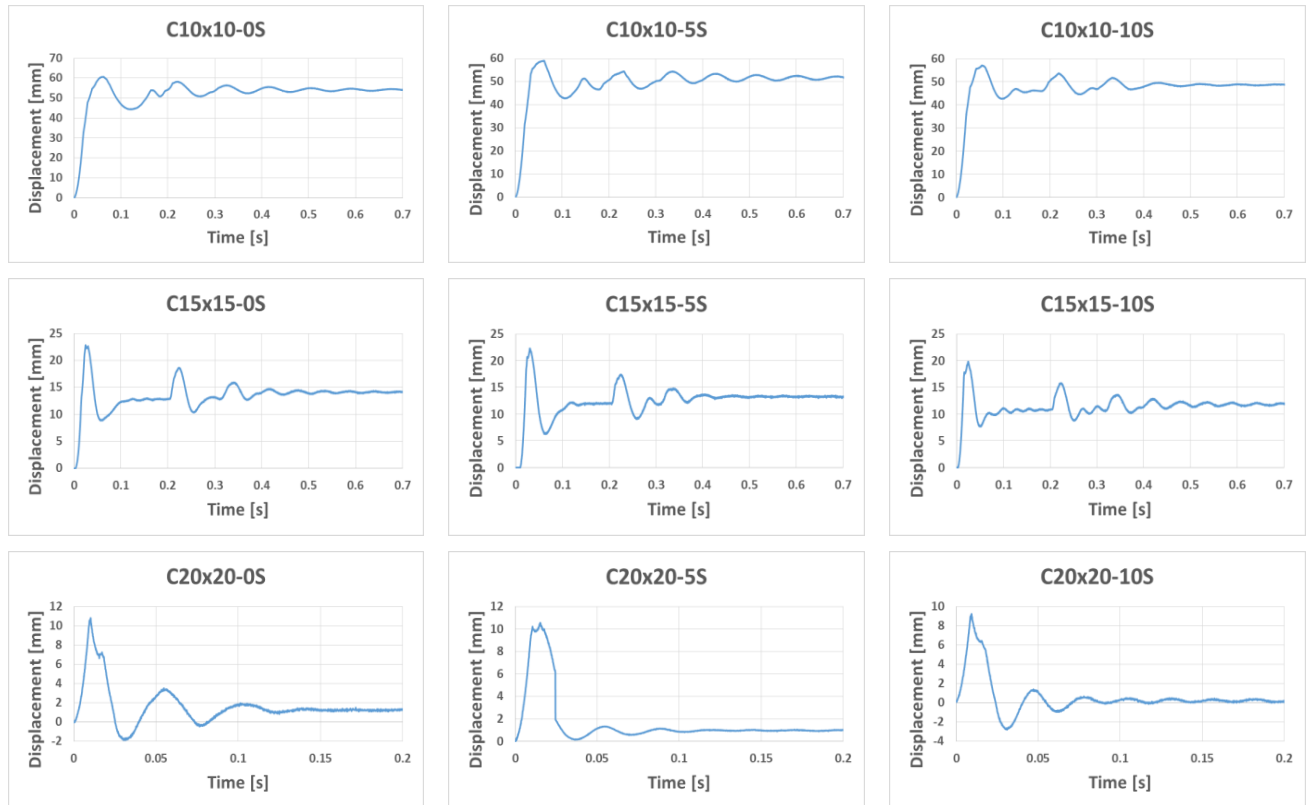


Fig. 7. Displacement – time graphs for all of the concrete bollards under impact loading.

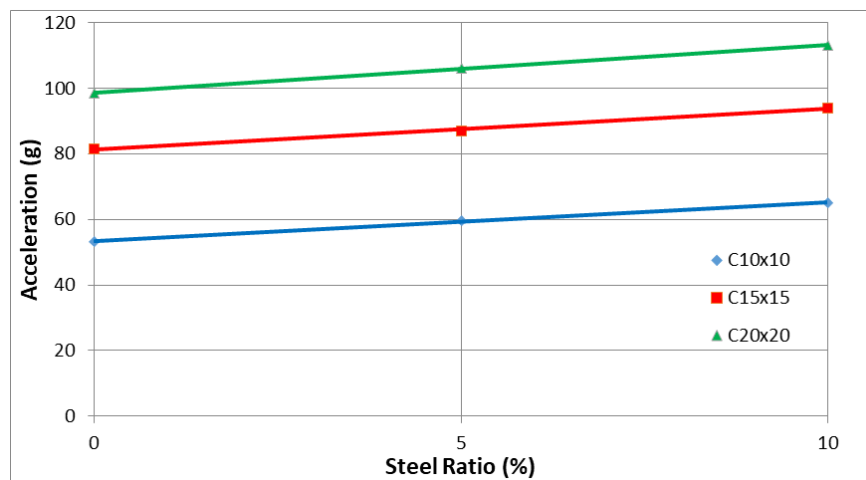


Fig. 8. Maximum average acceleration – steel ratio relationship obtained experimentally under impact loading.

Acceleration versus time graphs of the concrete bollards for all sections are given in Fig. 9.

3.3. Impact load – time graphs assessment

The impact load versus time graphs of the concrete bollards were acquired from the load cell on the top side of the specimen end. The impact load of the concrete bollards all exhibits a similar pattern with an initial peak point. Similarly, the initial peak is considerably bigger than subsequent peaks. The experimentally obtained impact load versus time graphs on the top side of the con-

crete bollards end are given in Fig. 10.

3.4. Deformation

The impact failures and the crack progressives of the 100x100 mm cross section specimens (by respectively 0%, 5% and 10% waste steel tire wire ratio) are given in Fig. 11. Whole crack initiation region is the support region of the concrete bollards. The crack size decrease with the waste steel tire wire ratio increase. It can be explained with the formation of crack bridges with the help of the steel wires and they slow down the crack.

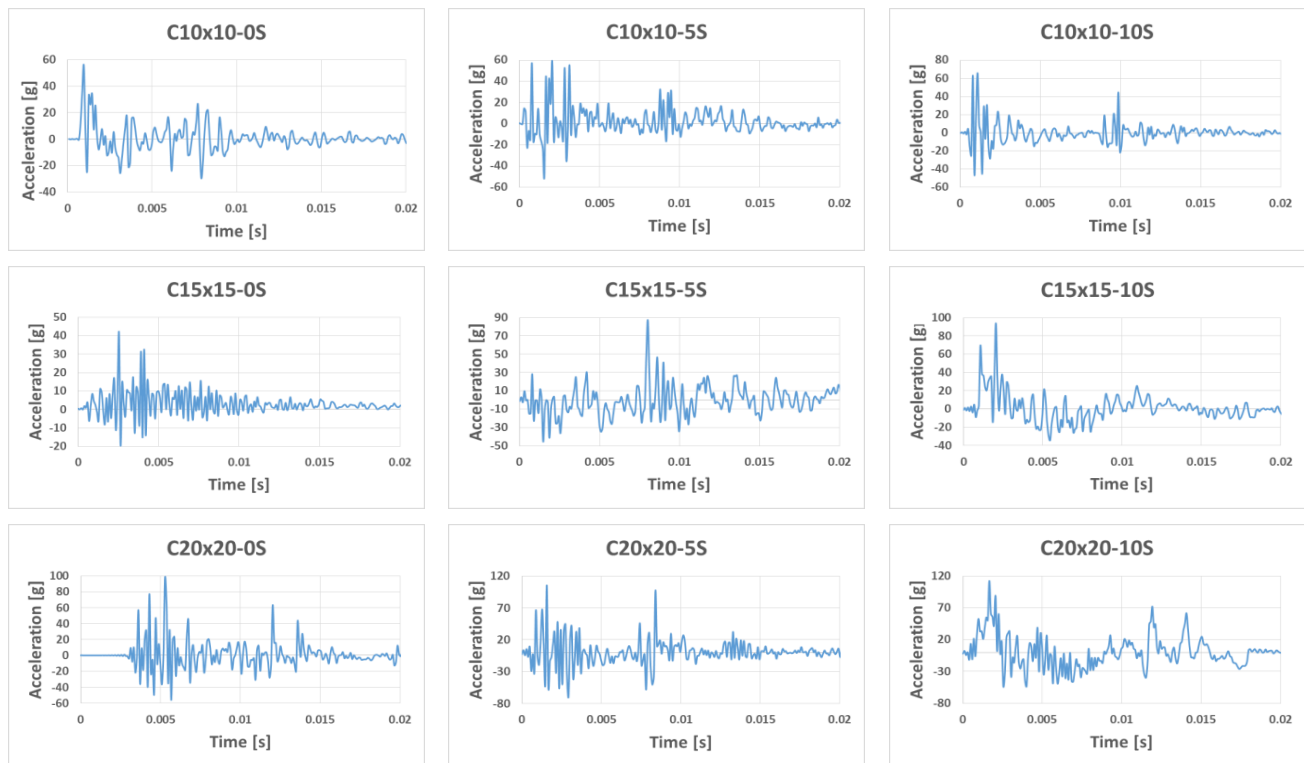


Fig. 9. Acceleration – time graphs for all of the concrete bollards under impact loading.

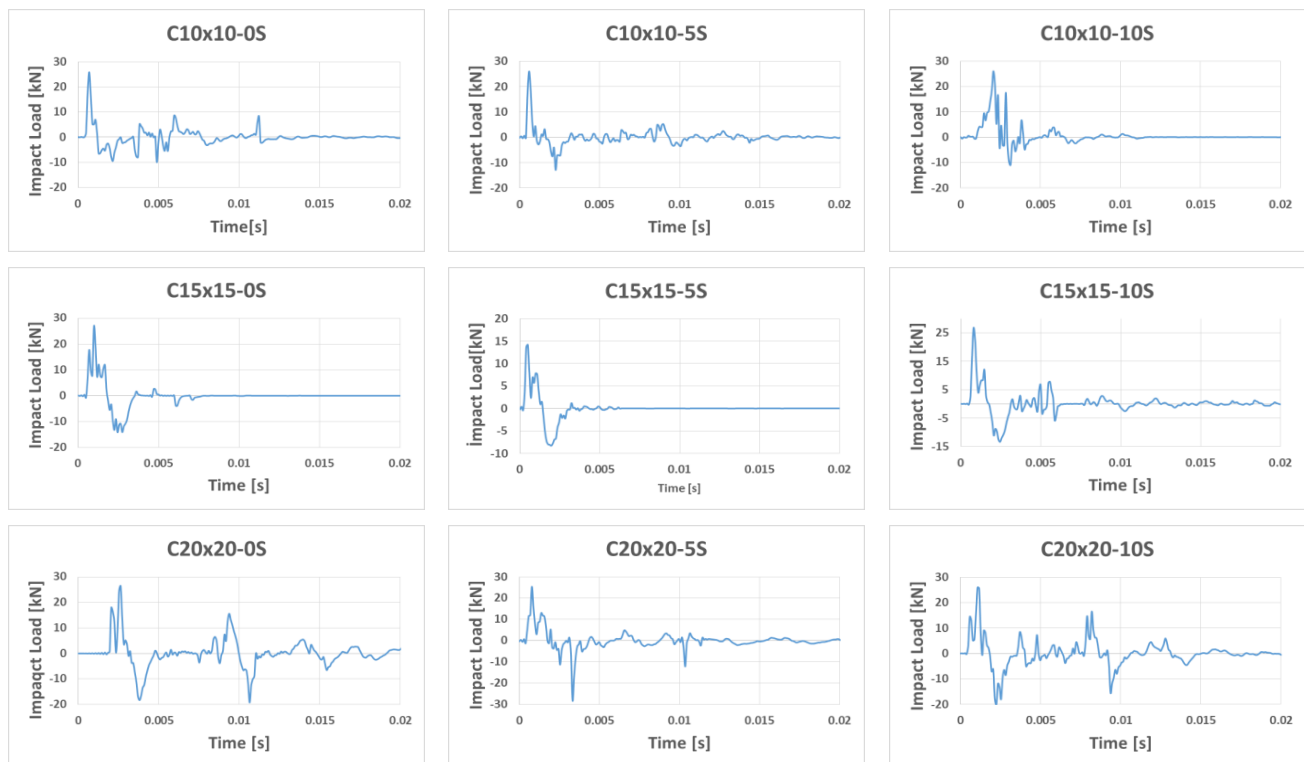


Fig. 10. Impact load – time graphs for all of the concrete bollards under impact loading.

The impact failures and the crack progressives of the 200x200 mm cross section specimens (by respectively 0%, 5% and 10% waste steel tire wire ratio) are given in Fig. 12. Crack initiation region is the support region of the concrete bollards as the same with other cross section specimens. The crack size decrease with the waste

steel tire wire ratio increase. It can be explained with the formation of crack bridges with the help of the steel wires and they slow down the crack.

Experimentally obtained results such as maximum deformation, residual deformation, maximum impact load and maximum average acceleration are given in Table 2.



Fig. 11. Failure of the C100x100 concrete bollards under impact loading.

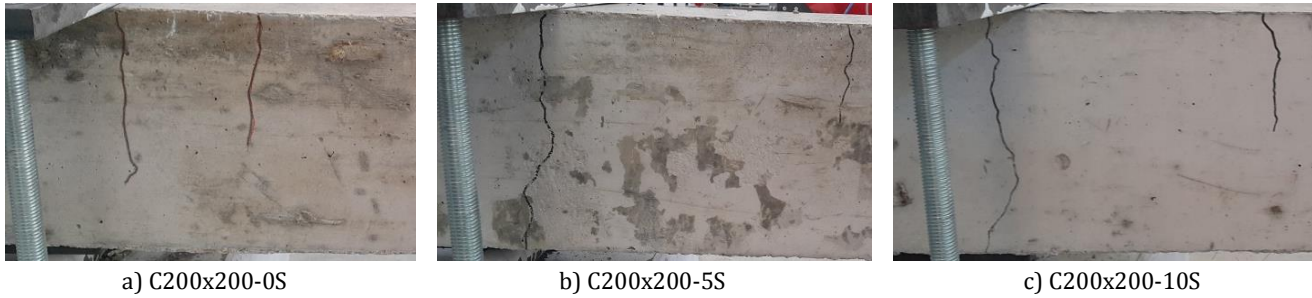


Fig. 12. Failure of the C200x200 concrete bollards under impact loading.

Table 2. Experimentally obtained test results.

Specimen	Maximum deformation (mm)	Residual deformation (mm)	Maximum impact load (kN)	Maximum average acceleration (m/sn^2)
C10x10x110R-%0S	60.72	54.15	25.86	53.3
C10x10x110R-%5S	59.10	51.69	25.92	59.6
C10x10x110R-%10S	57.10	48.66	26.02	64.9
C15x15x110R-%0S	22.83	14.11	26.79	81.6
C15x15x110R-%5S	22.30	13.27	14.16	87.0
C15x15x110R-%10S	19.80	11.80	26.68	93.9
C20x20x110R-%0S	10.80	1.23	26.45	98.5
C20x20x110R-%5S	10.50	1.13	26.40	106.2
C20x20x110R-%10S	9.20	0.92	26.01	113.1

4. Conclusions

The conclusions of this experimental study that investigated effect of waste steel tire wired concrete on the mechanical behavior under impact loading are summarized below.

- Specifications of the waste steel tire wires may not be equal such as thickness and length of wires. Steel wires recovered from waste tires also have some shredded rubber particulars in content. One more process may be useful to ensure the homogeneous and standardization of the steel wires recovered from waste tires.
- The maximum deformation of concrete bollards decreases as the waste steel tire wire ratio increases. Thus, as their capacity increases, they have more ability of deformation. They have a greater impact load carrying capacity.

- As the added volume of the steel wires recovered from waste tires increases, the workability decreases.
- Promising results are obtained by adding steel wires recycled from waste tires to concrete bollards, in terms of impact resistance,
- In terms of sustainability and a cleaner nature for posterity, recycling should be increased in our lives.

The experimental test aimed to research the effect of waste steel tire wired concrete on the mechanical behavior under impact loading as a possible environmentally friendly and sustainable solution. It can be said that the results provide the potential usage of waste steel tire wire manufacturing friendly to nature concrete bollards. Utilization of waste steel tire wire contributes to the sustainability of the concrete bollards. And also it is possible to enhance the productivity with more research. The effect of waste steel tire wire alignment during placing can be considered for further investigation. The more waste

steel tire wire ratio can be studied for better applicability and acceptability of this material. Since concrete bollards can be exposed to aggressive environmental conditions, their durability should also be considered in future studies. It also needs to be investigated under dynamic and static loading conditions. Generally, the usage of waste steel tire wire in concrete could be an innovative method in the construction industry.

Acknowledgements

None declared.

Funding

The authors received no financial support for the research, authorship, and/or publication of this manuscript.

Conflict of Interest

The authors declared no potential conflicts of interest with respect to the research, authorship, and/or publication of this manuscript.



REFERENCES

- Aiello MA, Leuzzi F, Centonze G, Maffezzoli A (2009). Use of steel fibres recovered from waste tyres as reinforcement in concrete: Pull-out behaviour, compressive and flexural strength. *Waste Management*, 29(6), 1960–1970.
- Faghih F, Das D, Ayoub A (2017). Seismic behavior of fiber reinforced steel-concrete composite systems. *Procedia Engineering*, 171, 899–908.
- Hannant DJ (2003). Fibre-reinforced concrete. *Advanced Concrete Technology - Processes*, 6/1-6/17.
- Lo Presti D (2013). Recycled tyre rubber modified bitumens for road asphalt mixtures: A literature review. *Construction and Building Materials*, 49, 863–881.
- Mastali M, Dalvand A, Sattarifard AR, Abdollahnejad Z, Illikainen M (2018). Characterization and optimization of hardened properties of self-consolidating concrete incorporating recycled steel, industrial steel, polypropylene and hybrid fibers. *Composites Part B: Engineering*, 151, 186–200.
- Mastali M, Dalvand A, Sattarifard AR, Abdollahnejad Z, Nematollahi B, Sanjayan JG, Illikainen M (2019). A comparison of the effects of poz-zolanic binders on the hardened-state properties of high-strength cementitious composites reinforced with waste tire fibers. *Composites Part B: Engineering*, 162, 134–153.
- Senesavath S, Salem A, Kashkash S, Zehra B, Orban Z (2021). The effect of recycled tyre steel fibers on the properties of concrete. *Pollack Periodica*, Accepted manuscript/Online first.
- Siraj N (2009). Steel Fiber Reinforced Concrete made with Fibers Extracted from Waste Tyres. *M.Sc. thesis*, Addis Ababa University, Ethiopia.
- Şengül Ö (2016). Mechanical behavior of concretes containing waste steel fibers recovered from scrap tires. *Construction and Building Materials*, 122, 649–658.
- Zeynal E (2008). Çelik Lif ve S/Ç Oranlarının Çelik Lifli Betonların Darbe Mukavemetine ve Mekanik Özelliklerine Etkisi. *M.Sc. thesis*, Ege University, İzmir. (in Turkish)



Research Article

Design and finite element analysis of a novel auxetic structure

Suleyman Nazif Orhan ^{a,*} , Şeydanur Erden ^a 

^a Department of Civil Engineering, Erzurum Technical University, 25050 Erzurum, Türkiye

ABSTRACT

In this study, a novel auxetic structure, namely RDN, is presented in two- and three-dimensions. The unit cells are created by modifying the conventional re-entrant structure and the 2D and 3D structures are formed by multiplying these unit cells. Finite element analyses are conducted to study the deformation mechanism of these structures under uniaxial tension, and the mechanical properties of the structures are obtained. Also, a 3D unit cell is modelled with different strut thickness values to examine the effect of the strut thickness on mechanical properties. Numerical models are developed using ANSYS/Static Structural software and linear elastic analyses are performed by applying small displacements to the structures. It is found that the 2D and 3D RDN structures possess a high negative Poisson's ratio but relatively small stiffness compared to the other auxetics. The analyses of the 3D unit cells showed that increasing the strut thickness led to higher stiffness values but reduced auxetic behaviour of the structure.

ARTICLE INFO

Article history:

Received 24 June 2022

Revised 13 July 2022

Accepted 8 August 2022

Keywords:

Negative Poisson's ratio

Auxetic

Finite element analysis

Stiffness

1. Introduction

Auxetic structures or materials are characterised by negative Poisson's ratio and contrary to traditional materials, expand due to tensile forces and contract with compressive effects (Fu et al. 2016; Wang et al. 2016). When compared to common materials, auxetic structures have many enhanced and unique mechanical properties such as fracture toughness, energy absorption and synclastic curvature due to their unusual deformation behaviour (Wang et al. 2018; Quan et al. 2020). These features make auxetics attractive for many practical applications such as biomaterials (Kuribayashi et al. 2006; Ali et al. 2014; Kolken et al. 2018; Yao et al. 2021), protective devices (Foster et al. 2018; Krishnan et al. 2021), civil engineering (Assidi and Ganghoffer 2012; Dhana-sekar et al. 2016; Zahra and Dhanasekar 2017), sensors (Xu et al. 1999; Ko et al. 2015), aerospace (Liu 2006; Ajaj et al. 2016), and so on.

Although auxetic materials can be found in nature, research into these materials has typically concentrated on manmade structures and started from the pioneering work carried out by Lakes (1987) (Wang et al. 2016; Shepherd et al. 2020). Following Lakes' seminal work,

two-dimensional (2D) artificial auxetic structures have experienced remarkable development and the achievements in these 2D structures have provided a great understanding of the nature of the unusual materials. However, with the development of fabrication techniques, three-dimensional (3D) auxetics attracted considerable interest and researchers have triggered a trend to develop more complex 3D models in recent years (Fu et al. 2016; Wang et al. 2018; Gao et al. 2021). Some papers in the literature have examined the mechanical properties of the various existing auxetic structures, while other studies have been carried out to expand the family of auxetic structures and explore potential applications of these structures. Among these studies, Fu et al. (2016) developed a novel 3D re-entrant structure that can achieve a negative Poisson's ratio in two principal orthogonal directions. Lu et al. (2017) proposed two novel auxetic 3D chiral structures based on the 2D cross chiral structure and confirmed that the combined structures have a higher Young's modulus. A new structure named re-entrant chiral auxetic (RCA) was proposed by Alomarah et al. (2019) based on the re-entrant and chiral structures. They compared mechanical properties of this structure with three different auxetic honeycombs and

* Corresponding author. Tel.: 444-5-388 ; Fax: +90-442-230-0036 ; E-mail address: s.orhan@erzurum.edu.tr (S. N. Orhan)

stated that the RCA structure offered better energy absorption capacity than the other three auxetics. Qi et al. (2020) replaced the sloped cell wall of a re-entrant hexagonal honeycomb with a double circular arch cell wall and proposed a novel re-entrant circular (REC) structure. The specific energy absorption of the REC structure was found to be much higher than that of the regular re-entrant honeycomb. Su et al. (2020) proposed a unique re-entrant honeycomb structure with reinforcement arches to achieve better structural stiffness while retaining the auxetic behaviour of the structure. Wei et al. (2020) developed a new 3D anti-tetrachiral auxetic and investigated the deformation characteristic of the structure. They found that one of the Poisson's ratios is independent of the geometric parameters. Gao et al. (2021) proposed a class of novel 3D auxetic structures based on the rigid rotating mechanism. They stated that these structures are capable of offering a Poisson's ratio from positive to negative in a wide range along the three principal axes and are suitable for many engineering applications.

As can be seen from the above literature, various researches have been conducted to create new auxetics by modifying the geometries of existing ones. In this paper, a new auxetic lattice structure, namely RDN, was pro-

posed in two- and three-dimensions based on the corresponding re-entrant auxetic topology. The behaviour of these structures under tensile effects was investigated with FEM-based (finite element method) analyses using ANSYS software. From the numerical analyses, stiffness and Poisson's ratio values of these structures were calculated and compared with other auxetic structures. Moreover, the 3D unit cell of the structure was modelled by varying the thickness of the struts between 0.5 and 1.5 mm to investigate the influence of strut thickness on auxetic behaviour. Finally, von Mises stress distributions on the structures were examined.

2. Design and Analysis

The RDN structure was designed based on the 2D re-entrant structure geometry. By modifying the 2D re-entrant auxetic, first a 2D unit cell consisting of diagonal and horizontal ligaments was designed, and then a three-dimensional unit cell was modelled (Fig. 1).

The 2D and 3D unit cells were constructed by CAD software SolidWorks 2016 (Dassault Systems, Massachusetts, USA) and by combining the unit cells, two- and three-dimensional structures were obtained as seen in Fig. 2.

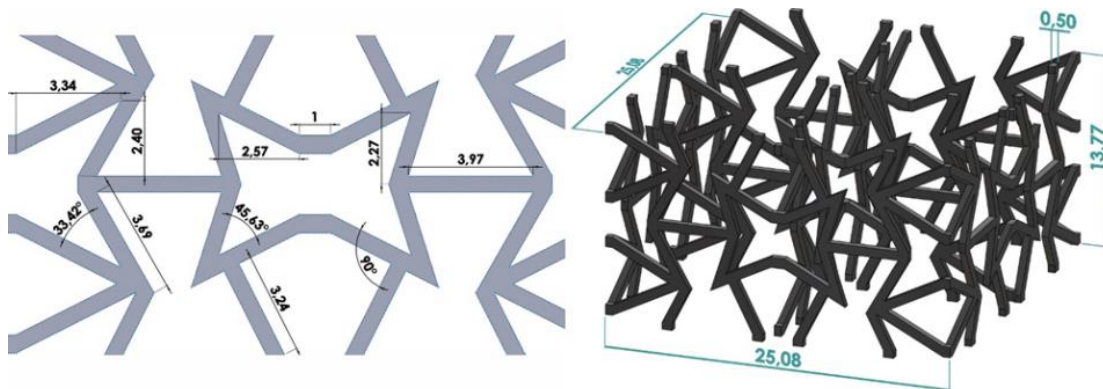


Fig. 1. Two- and three-dimensional RDN unit cells (all dimensions in mm).

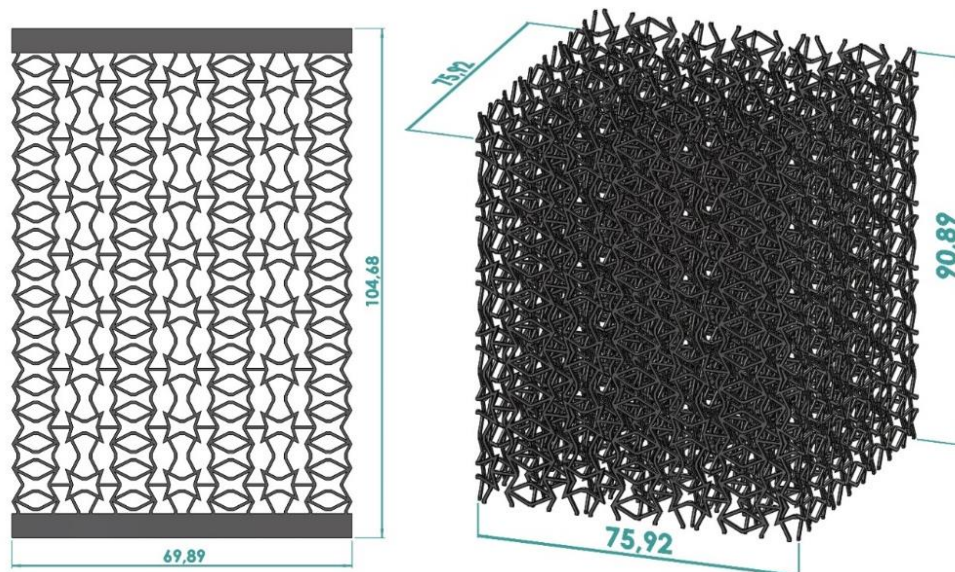


Fig. 2. Two- and three-dimensional RDN structures (all dimensions in mm).

In modelling these structures, the dimensions of our previously examined auxetic structures (Orhan and Erden 2022) were taken into account. Thus, the mechanical properties were intended to be comparable. Finite element analyses were conducted to examine the behaviour of these structures under displacements as uniaxial tension and the stiffness and Poisson's ratio of the structures were determined. Besides, the 3D unit cells were modelled with four different strut thickness values (0.5, 1, 1.2 and 1.5 mm) to explore the effect of strut thickness on the auxeticity of the RDN structure.

The numerical simulations of the structures were performed using the Static Structural analysis module of the ANSYS Workbench (v20.R1) (ANSYS Inc., PA, USA) software. To determine the mesh element size and the boundary conditions, the results of the validation and mesh convergence study we had previously performed and presented were taken into account. In our previous study (Orhan and Erden 2022), we modelled and analysed the re-entrant structures that were investigated numerically and experimentally by Wang et al. (2016) and compared the results to validate our models. Detailed information about these analyses was given in our previous paper. In line with the results obtained from the

validation study, the boundary conditions applied in the analyses are shown in Fig. 3. All structures were fixed from one side and a constant displacement was applied to the other side. Two platens of thickness 5 mm, were placed to the top and bottom sides of the 3D structure and platens were fixed on the structure employing "bonded" contact. In the 3D unit cells, fixation and loading were made directly on the surface of the struts, and no platens were used. Displacement values were taken as 1/1000 of the structures' heights ($\varepsilon_y \leq 0.001$) to conduct analyses in the linear elastic region. In the analyses, all structures were meshed with hexahedron (hex20) elements and the selected mesh size was of 0.67 mm following our previous mesh convergence study. The "structural steel" from the ANSYS material library was defined as material for all RDN structures in the analysis (Table 1).

Considering the points seen in Fig. 3 and using Eqs. (1) and (2) given below, the Poisson's ratio (ν_{yx}) of each RDN auxetic was determined. Also, the force values corresponding to the applied displacements were obtained for each structure and force-displacement curves were created. The stiffness of the auxetics was derived from the slope of these curves.

Table 1. Material properties used in numerical analysis.

Material	Density	Young's modulus	Poisson's ratio	Tensile yield strength	Tensile ultimate strength
Structural steel	7.85 gr/cm ³	200 GPa	0.3	0.25 GPa	0.46 GPa

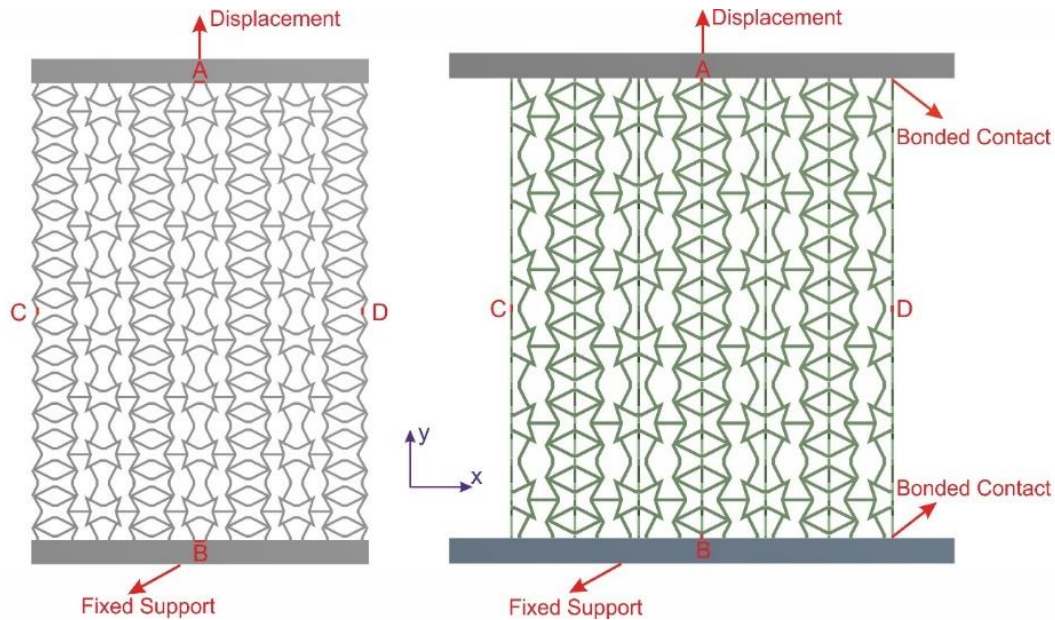


Fig. 3. Boundary conditions used in FEM analysis.

$$\varepsilon_x = \frac{\Delta L_x}{L_x}, \quad \varepsilon_y = \frac{\Delta L_y}{L_y}$$

$$\nu_{yx} = -\frac{\varepsilon_x}{\varepsilon_y}$$

- (1) where, ε_y is the strain calculated in the longitudinal direction, ε_x is the strain calculated in the lateral direction, L_x and L_y are the original distances between points C-D and A-B, respectively, and ΔL_x and ΔL_y are the change in distances between these points after deformation.
- (2)

3. Results and Discussion

The force-displacement curves generated from the analyses of the two- and three-dimensional RDN structures are illustrated in Fig. 4 and the stiffness and Poisson's ratio values of the structures are given in Table 2.

From these results, it is seen that the 2D and 3D RDN structures showed auxetic behaviour as desired and had a high negative Poisson's ratio. When these results were

compared with the previously examined re-entrant, lozenge grid, arrowhead and elliptic hole structures (Orhan and Erden 2022), the stiffness and Poisson's ratio values of the 2D RDN were found to be larger than the values obtained from the re-entrant and lozenge grid structures. In three dimensions, it is determined that the Poisson's ratio of the RDN structure was larger than those of the re-entrant and lozenge grid structures, and the stiffness value was smaller than that of the other four auxetics.

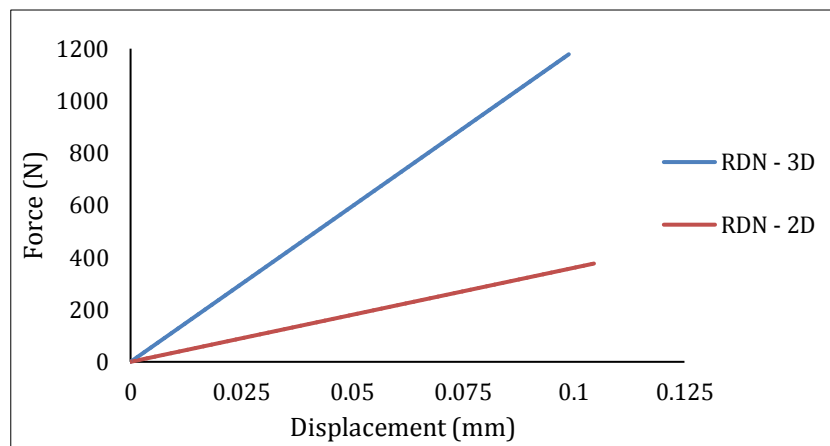


Fig. 4. Force-displacement curves of the RDN structures.

Table 2. Mechanical properties of the RDN structures obtained from the analyses.

Auxetic	Stiffness (N/mm)		Poisson's Ratio	
	2D	3D	2D	3D
RDN	3601	11916	-0.704	-0.806

When the von Mises stresses at the 2D and 3D RDN auxetics were examined, it was seen that the maximum von Mises stresses occurred at the corner points where the longitudinal struts are connected to the horizontal elements (Fig. 5). The highest von Mises stresses of 259.1 MPa and 212.8 MPa were found at the 2D and 3D structures, respectively. In order to reduce the stress concentration, the edges can be substituted by curves.

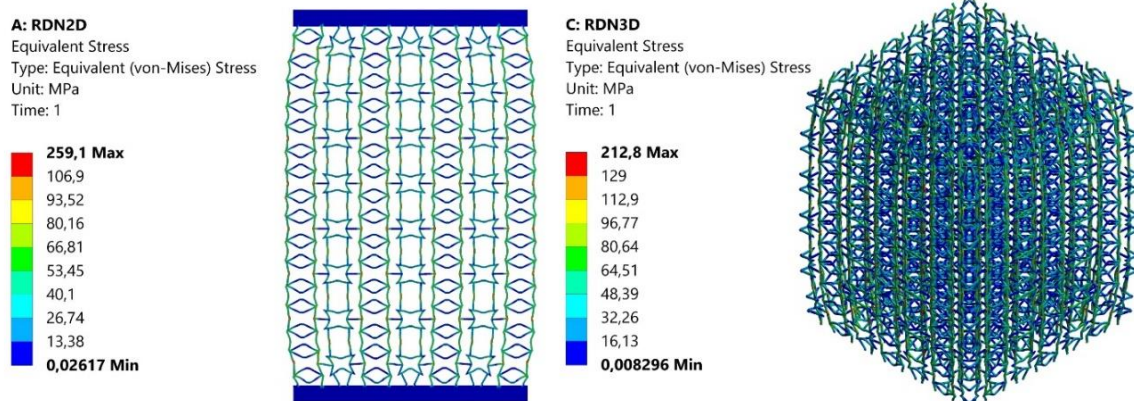


Fig. 5. Maximum von Mises stresses at the RDN structures.

The force-displacement curves obtained from the analyses of the 3D unit cells modelled with different strut thickness values are shown in Fig. 6. The Poisson's ratio, relative density and stiffness values of these unit cells are also given in Table 3. It is found that the Poisson's ratio decreases from -0.793 to -0.663 and stiffness increases from 22876 N/mm to 60874 N/mm with an increase of thickness from 0.5 mm to 1.5 mm. Although in

a study conducted by Meena et al. (2019), it was stated that the thickness had no discernible effect on the auxetic behaviour of the structure, our results were consistent with other studies where it was indicated that the Poisson's ratio of the auxetic structure decreases with increase of strut thickness (Lee et al. 1996; Schwerdtfeger et al. 2012; Ren et al. 2015). The Poisson's ratio and stiffness values versus strut thickness are plotted in Fig. 7.

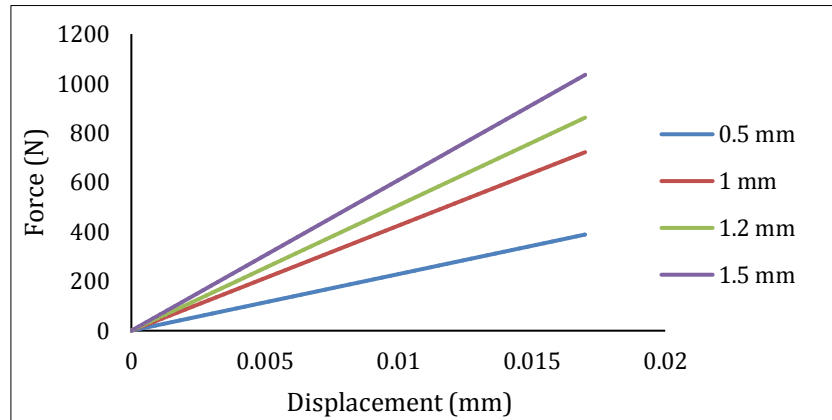


Fig. 6. Force-displacement curves of the 3D RDN unit cells.

Table 3. The effect of strut thickness on the mechanical properties of the unit cell.

Strut thickness (mm)	Poisson's ratio	Stiffness (N/mm)	Relative density (%)
0.5	-0.793	22876	0.0321
1.0	-0.721	42475	0.0508
1.2	-0.688	50694	0.0616
1.5	-0.663	60874	0.0716

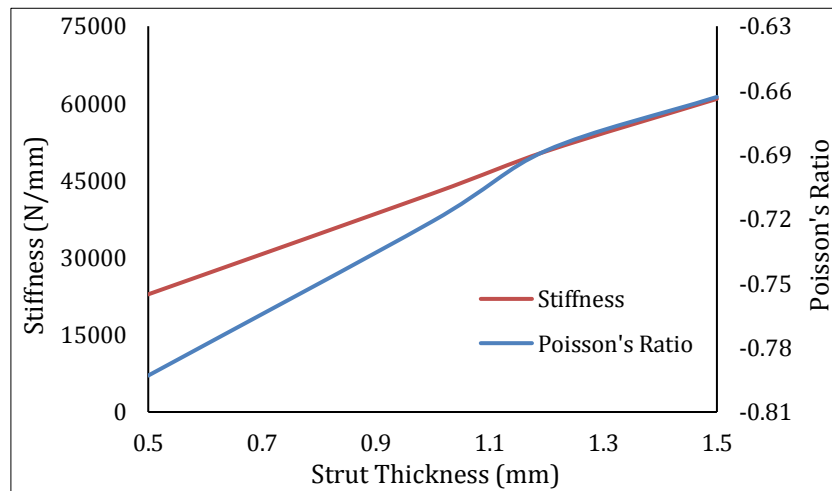


Fig. 7. Poisson's ratio and stiffness change with strut thickness.

Fig. 8 shows the stress distribution along the 3D unit cells with different strut thicknesses. The maximum von Mises stress was obtained as 347 MPa at the unit cell with 0.5 mm strut thickness. As the strut thickness and the relative density of the unit cell increased, the stress

values gradually decreased. Hence, the largest stress was determined as 305.5 MPa for the unit cell with 1.5 mm strut thickness. The percentage change of the maximum von Mises stress with respect to the change of strut thickness is shown in the Table 4.

Table 4. Change of the maximum von Mises stress with increasing strut thickness.

	Strut thickness (mm)			
	0.5	1	1.2	1.5
Percentage increase of the strut thickness (%)	100	140	200	
Maximum von Mises stress (MPa)	347	333.3	321.6	305.5
Percentage decrease of the maximum von Mises stress (%)		3.95	7.32	11.96

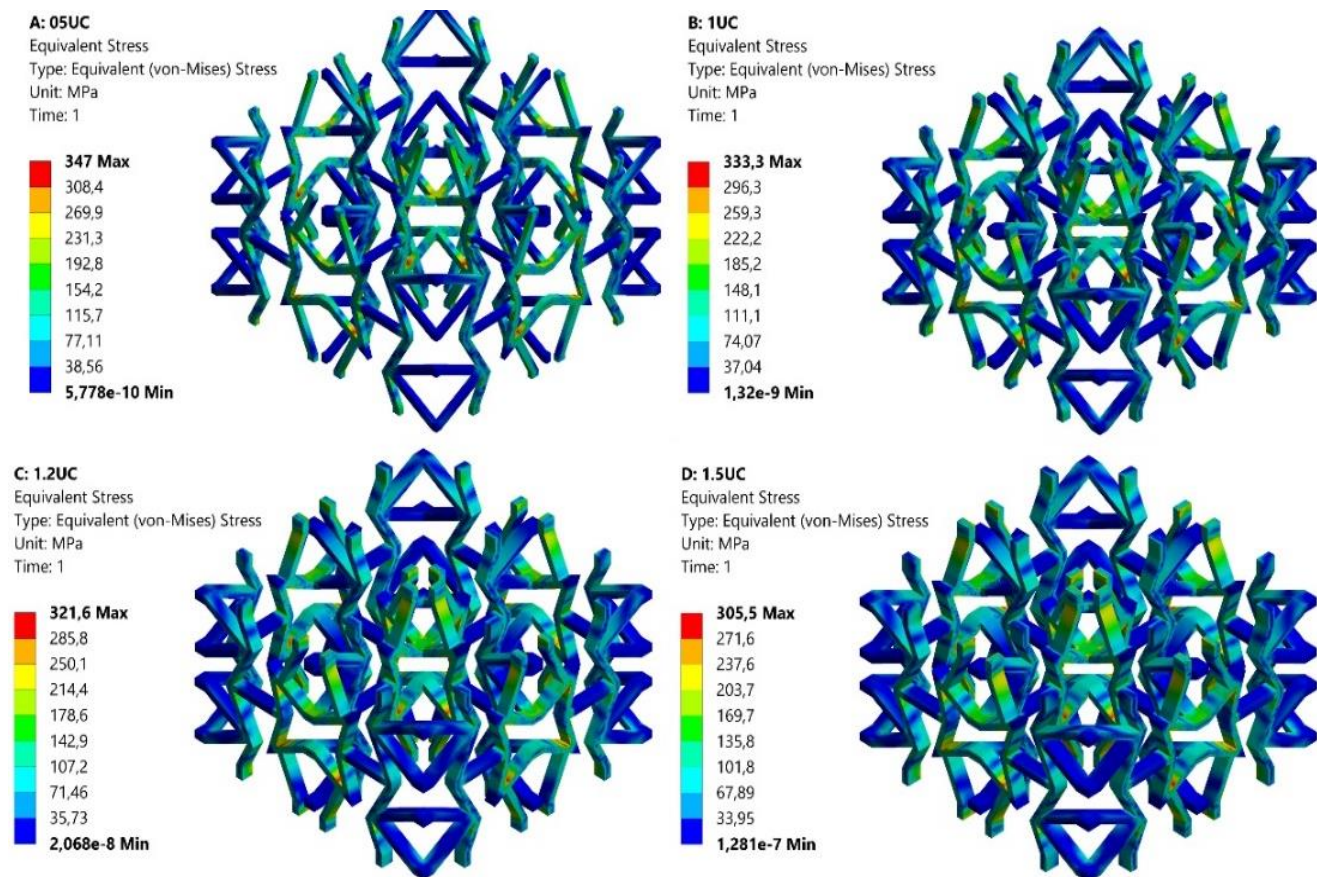


Fig. 8. Maximum von Mises stress distributions at the 3D unit cells.

4. Conclusions

In this present work, a new auxetic lattice structure was proposed in two- and three-dimensions. The design of this structure was carried out by modifying the conventional re-entrant auxetic. Finite element analyses were conducted under axial extension to determine the mechanical properties and the deformation characteristics of these structures. The analyses showed that the structures are capable of offering auxetic behaviour and a high negative Poisson's ratio. It was found that the Poisson's ratio of the 3D RDN auxetic was greater than the lozenge grid and re-entrant structures but the stiffness of the structure was lower when compared with the re-entrant, lozenge grid, arrowhead and elliptic hole structures. However, this design is the first step for the RDN structure. Considering the stress distribution in the structure, the unit cell modifications and shape optimisation can be performed, and the mechanical performance of the structures can be enhanced. In addition, analyses can be carried out under both quasi-static and dynamic compression loads to determine other mechanical properties of the structure, like compressive and buckling strength. Furthermore, experimental investigation of the presented structures could be performed and the possible application of the structure in different fields such as biomedicine or civil engineering could be determined in future works.

Acknowledgements

None declared.

Funding

The authors received no financial support for the research, authorship, and/or publication of this manuscript.

Conflict of Interest

The authors declared no potential conflicts of interest with respect to the research, authorship, and/or publication of this manuscript.

REFERENCES

- Ajaj RM, Beaverstock CS, Friswell MI (2016). Morphing aircraft: The need for a new design philosophy. *Aerospace Science and Technology*, 49, 154-166.
- Ali MN, Busfield JJC, Rehman IU (2014). Auxetic oesophageal stents: structure and mechanical properties. *Journal of Materials Science-Materials in Medicine*, 25(2), 527-553.

- Alomarah A, Ruan D, Masood S, Gao Z (2019). Compressive properties of a novel additively manufactured 3D auxetic structure. *Smart Materials and Structures*, 28(8), 085019.
- Assidi M, Ganghoffer JF (2012). Composites with auxetic inclusions showing both an auxetic behavior and enhancement of their mechanical properties. *Composite Structures*, 94(8), 2373-2382.
- Dhanasekar M, Thambiratnam DP, Chan THT, Noor-E-Khuda S, Zahra T (2016). Modelling of masonry walls rendered with auxetic foam layers against vehicular impacts. *Brick and Block Masonry: Trends, Innovations and Challenges*, Padova, Italy, 977-983.
- Foster L, Peketi P, Allen T, Senior T, Duncan O, Alderson A (2018). Application of auxetic foam in sports helmets. *Applied Sciences-Basel*, 8(3), 354.
- Fu MH, Chen Y, Zhang WZ, Zheng BB (2016). Experimental and numerical analysis of a novel three-dimensional auxetic metamaterial. *Physica Status Solidi B-Basic Solid State Physics*, 253(8), 1565-1575.
- Gao Y, Wei XY, Han XK, Zhou ZG, Xiong J (2021). Novel 3D auxetic lattice structures developed based on the rotating rigid mechanism. *International Journal of Solids and Structures*, 233, 111232.
- Ko J, Bhullar S, Cho YY, Lee PC, Jun MBG (2015). Design and fabrication of auxetic stretchable force sensor for hand rehabilitation. *Smart Materials and Structures*, 24(7), 075027.
- Kolken HMA, Janbaz S, Leeftang SMA, Lietaert K, Weinans HH, Zadpoor AA (2018). Rationally designed meta-implants: a combination of auxetic and conventional meta-biomaterials. *Materials Horizons*, 5(1), 28-35.
- Krishnan BR, Biswas AN, Kumar KVA, Sreekanth PSR (2021). Auxetic structure metamaterial for crash safety of sports helmet. *Materials Today: Proceedings*, 56(3), 1043-1049.
- Kuribayashi K, Tsuchiya K, You Z, Tomus D, Umemoto M, Ito T, Sasaki M (2006). Self-deployable origami stent grafts as a biomedical application of Ni-rich TiNi shape memory alloy foil. *Materials Science and Engineering a-Structural Materials Properties Microstructure and Processing*, 419(1-2), 131-137.
- Lakes R (1987). Foam structures with a negative Poisson's ratio. *Science*, 235(4792), 1038-1040.
- Lee J, Choi JB, Choi K (1996). Application of homogenization FEM analysis to regular and re-entrant honeycomb structures. *Journal of Materials Science*, 31, 4105-4110.
- Liu Q (2006). Literature review: Materials with negative Poisson's ratios and potential applications to aerospace and defence. *Defence Science and Technology Organisation*, Victoria, Australia.
- Lu Z, Wang Q, Li X, Yang Z (2017). Elastic properties of two novel auxetic 3D cellular structures. *International Journal of Solids and Structures*, 124, 46-56.
- Meena K, Calius EP, Singamneni S (2019). An enhanced square-grid structure for additive manufacturing and improved auxetic responses. *International Journal of Mechanics and Materials in Design*, 15, 413-426.
- Orhan SN, Erden S (2022). Numerical investigation of the mechanical properties of 2D and 3D auxetic structures. *Smart Materials and Structures*, 31(6), 065011.
- Qi C, Jiang F, Remennikov A, Pei LZ, Liu J, Wang JS, Liao XW, Yang S (2020). Quasi-static crushing behavior of novel re-entrant circular auxetic honeycombs. *Composites Part B: Engineering*, 197, 108117.
- Quan C, Han B, Hou ZH, Zhang Q, Tian XY, Lu TJ (2020). 3d printed continuous fiber reinforced composite auxetic honeycomb structures. *Composites Part B-Engineering*, 187, 107858.
- Ren X, Shen J, Ghaedizadeh A, Tian H, Xie YM (2015). Experiments and parametric studies on 3D metallic auxetic metamaterials with tuneable mechanical properties. *Smart Materials and Structures*, 24(9), 095016.
- Schwerdtfeger J, Schury F, Stingl M, Wein F, Singer RF, Körner C (2012). Mechanical characterisation of a periodic auxetic structure produced by SEBM. *Physica Status Solidi B-Basic Solid State Physics*, 249(7), 1347-1352.
- Shepherd T, Winwood K, Venkatraman P, Alderson A, Allen T (2020). Validation of a finite element modeling process for auxetic structures under impact. *Physica Status Solidi B-Basic Solid State Physics*, 257(10).
- Su Y, Wu X, Shi J (2020). A novel 3D printable multimaterial auxetic metamaterial with reinforced structure: Improved stiffness and retained auxetic behavior. *Mechanics of Advanced Materials and Structures*, 29(3), 408-418.
- Wang XT, Li XW, Ma L (2016). Interlocking assembled 3D auxetic cellular structures. *Materials & Design*, 99, 467-476.
- Wang XT, Wang B, Wen ZH, Ma L (2018). Fabrication and mechanical properties of CFRP composite three-dimensional double-arrow-head auxetic structures. *Composites Science and Technology*, 164, 92-102.
- Wei YL, Yang QS, Liu X, Tao R (2020). A novel 3D anti-tetrachiral structure with negative Poisson's ratio. *Smart Materials and Structures*, 29(8), 085003.
- Xu B, Arias F, Brittain ST, Zhao XM, Grzybowski B, Torquato S, Whitesides GM (1999). Making negative Poisson's ratio microstructures by soft lithography. *Advanced Materials*, 11(14), 1186-1189.
- Yao Y, Yuan H, Huang HW, Liu JL, Wang LZ, Fan YB (2021). Biomechanical design and analysis of auxetic pedicle screw to resist loosening. *Computers in Biology and Medicine*, 133, 104386.
- Zahra T, Dhanasekar M (2017). Characterisation of cementitious polymer mortar - Auxetic foam composites. *Construction and Building Materials*, 147, 143-159.



Research Article

Boundary plate influence on tie bars axial force demands in composite plate shear walls–concrete filled

Erkan Polat ^{a,*} 

^a Department of Civil Engineering, Munzur University, 62000 Tunceli, Türkiye

ABSTRACT

In composite plate shear walls–concrete filled (C-PSW/CF), there is an indeterminate flow of force between concrete, steel plate and tie bars. Finite element methods (FEM) are frequently used to verify this force flow. The theoretical models available in the literature to predict the tie bar maximum axial force demands were based on walls without boundary plates. The finding in this study is intended to help understand whether current theoretical approaches are conservative and can be applied to boundary plate walls as well. Within the scope of this study, tie bar axial force demands for walls with boundary plates consisting of planar and round shapes and without boundary plates were investigated and compared. For this, a previously benchmarked finite element (FE) wall model was considered and configured to have no boundary plate and have planar and round boundary plates. FE models were analyzed under monotonic lateral displacement up to 4% drift ratio. Passive lateral pressures and transverse force variations on the planar and round boundary plates were investigated.

ARTICLE INFO

Article history:

Received 1 June 2022

Revised 25 August 2022

Accepted 23 September 2022

Keywords:

Composite plate shear walls

Concrete-filled

Tie bar

Boundary

Axial force

1. Introduction

In composite plate shear walls – concrete filled (C-PSW/CF) there is an indeterminate flow of forces between the wall parts (i.e., steel plates, infill concrete and tie bars). This force flow provides composite behavior and achieved by axial and shear force transfer between the wall parts. Axial and shear forces are transferred from concrete to steel plate or from steel plate to concrete by means of direct pressure and interface friction between the steel and the concrete, and also by the tie bars distributed along the wall surface at specified intervals.

Capacity-based design principles are followed in the design of C-PSW/CF. The wall is assumed to attain plastic moment capacity at the base: the steel plates are assumed to attain their yield strength, and the concrete is assumed to reach its unconfined compressive strength. Because of construction appeal such as modular construction, construction speed, functionally (being used as formwork, falsework) off-site fabrication, and structural appeal such as ductility, high-stiffness and strength,

C-PSW/CF have been extensively researched in the last two decades (e.g. Oduyemi and Wright (1989), Wright et al. (1991), Bowerman et al. (1999), Xie and Chapman (2006), Eom et al. (2009), Ramesh (2013), Alzeni and Bruneau (2017), Polat and Bruneau (2017, 2018), Varma et al. (2019), and Kenarangi et al. (2021)).

Polat and Bruneau (2018) showed that axial forces on the steel plate were redistributed to infill concrete following the steel plate local buckling. Polat et al. (2021) and Polat (2022) showed that tie bars axial force demands in planar C-PSW/CF result from the prying action of the steel plate and the confinement action of the infill concrete. The prying action is introduced by steel plate local buckling following yielding under wall flexural deformation and is related to prying length and through-thickness plastic moment of the steel plate. The concrete confinement action is introduced under wall flexure and large compressive strains developed within the concrete. Arching action is assumed to form within the concrete under compression between the adjacent tie bars in the vertical axis. Theoretical models were developed

* Corresponding author. Tel.: +90-428-213-1794 ; E-mail address: erkanpolat@munzur.edu.tr (E. Polat)

to predict the tie bars axial force demands due to prying action (Polat et al. 2021) and to predict the tie bars axial force demands due to confining action (Polat 2022). However, although the walls examined in these studies did not have boundary plates, in practice, boundary plates can often be preferred because they both increase the strength of the wall and form a formwork for concrete placement. This study aims to investigate the influence of round and planar boundary plates, which are frequently used for C-PSW/CF, on the axial force demands of the tie bars. In addition, this study shows that the theoretical models developed by Polat (2022) based on walls without boundary plates to predict tie bar maximum force demands are conservative and can also be applied for walls with boundary plates.

2. Wall Geometry and Properties

Fig. 1(a-c) illustrates the cross-sections of the wall models. Note that the wall model shown in (c) was designed and tested by Alzeni and Bruneau (2017) and was used as a reference for the other wall geometries shown in (a) and (b). Wall cross-sections consist of steel web plates, infill concrete and boundary plates. The location of the tie bars, extending between the dual steel web plates, are also indicated in the Figure. Model NB, shown in the Fig. 1(a), has no boundary plates. Models B1 and B2, shown in Fig. 1(b-c), have boundary elements in the form of planar and round plates, respectively. Except for

the boundary plates, the walls have otherwise the same geometry and dimensions.

Fig. 2 shows a representative wall dimension in elevation and plan view for Model NB. All Models has a height of 3048mm, infill concrete thickness of 203.2mm, steel web plate and boundary plate thickness (t_s) of 7.94mm, tie bar diameter of 25.4mm. The total depths of the cross-sections are 1016mm, 1025.5mm and 1235mm for Models NB, B1 and B2; respectively. The tie bars are spaced 203.2 mm horizontally (w_2) and vertically (w_1), except that the horizontal distance between the last two rows is 152.4 mm. The slenderness of the steel web plate given by the ratio of vertical tie spacing to plate thickness (w_1/t_s) equal to 25.6 for all Models. The reinforcement ratio (calculated as the ratio of steel area to concrete area) is 7.8%, 9.4%, and 8.96% for Models NB, B1 and B2, respectively. Accordingly, all Models have satisfactory reinforcement ratio with regards to AISC 341-22 Seismic Provisions (AISC 2022) where the reinforcement ratio for C-PSW/CF is limited to 1-10%.

The infill concrete has uniaxial compressive strength of 47.8 MPa. The steel web and boundary plates have a yield strength of 427 MPa, an elastic modulus of 205463 MPa. For the tie bars, elastic material properties were used. Note that six tie bars were identified in Fig. 1(a) and denoted as; Tie₁₁, Tie₁₂ for the first row Tie₂₁, Tie₂₂ for the second row, and Tie₃₁, Tie₃₂ for the third row. In Section 4, the axial force demand on these tie bars will be used to compare for Models NB, B1 and B2 under monotonic lateral displacement.

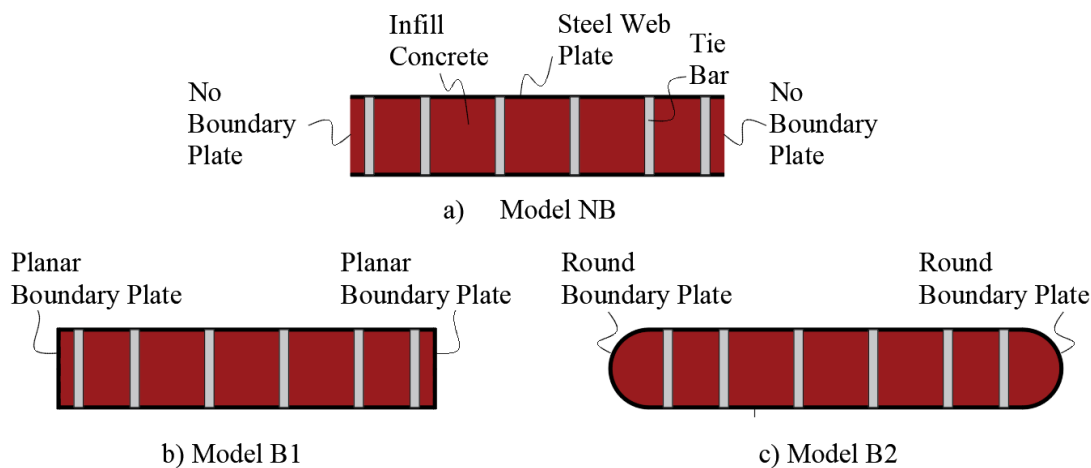


Fig. 1. Illustration of wall cross-sections: (a) Model NB; (b) Model B1; and (c) Model B2.

3. Finite Element Modeling

3.1. Element and material models

Finite element (FE) models of the walls were developed using LS-Dyna (LSTC 2022). Fig. 3 shows the isometric views of the developed FE models. Since the walls were symmetrical with respect to the loading direction, the walls were modeled only in half using the symmetry boundary conditions. In terms of elements, four node fully integrated shell element was used for modeling the web and boundary plates, eight node constant stress solid element was used to model the concrete and two

node beam element was used to model the tie bars. In terms of element sizes, each solid element was 25.4x25.4x25.4mm, each shell element was 25.4x25.5, and each beam element was 25.4mm. For modeling the tie bars, the slip model developed by Polat et al. (2021) was used. In this model, tie bars extending between the steel plates are restrained to infill concrete in the two orthogonal transverse directions (i.e., X and Z axes) and unrestrained in its own axis (i.e., Y axis); allowing development of uniform axial force along the tie bars. For typical half-symmetric FE model, for example for Model NB, a total of 19200 solid elements, 4800 shell elements, and 360 beam elements were used.

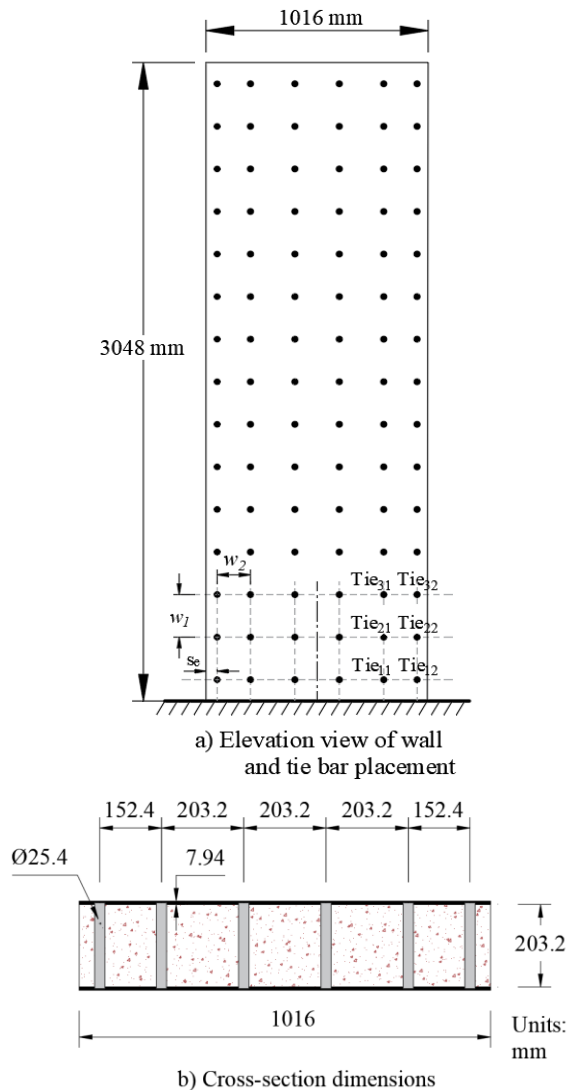


Fig. 2. Dimensions of Model NB in: (a) Elevation view of wall and tie bar placement; and (b) Cross-section.

For modeling the concrete, the Karagozian & Case Concrete Model – Release III (KCC) was used. The selection of this model is based on prior studies (Polat 2020; Polat et al. 2021) that have shown that walls with KCC can reasonably predict the ultimate strength of the walls tested while simulating concrete dilation. For modeling the steel, the plastic-kinematic material model was used. This model is represented by bi-linear curves with elastic and post-elastic modulus. The same material model with elastic properties was used for modeling the tie bars. Note that, Model B2 was developed previously with base footing (with different concrete material model and without tie bar slip model) by Polat and Bruneau (2017) and benchmarked against tested specimen (Alzeni and Bruneau 2014; Alzeni and Bruneau 2017). Model NB is the same model considered in the investigation of tie bars axial force demands in C-PSW/CF without boundary plates by Polat et al. (2021).

3.2. Finite element analysis

The Models were subjected to static displacement at the top. Implicit solution procedure of the program was used for the inelastic nonlinear analysis of the Models. The maximum time step for the nonlinear analysis was set to 0.01second (resulting in hundred steps for a total of 1 second loading curve). Using 4-core dedicated processors, a typical analysis duration was about two hours. Fig. 4(a-c) shows the pushover curves of the walls under monotonic lateral displacement. The maximum lateral load carrying capacity was 917 kN for Model NB, 1265 kN for Model B1, and 1660 kN for Model B2. Model NB exhibited gradual strength degradation as a result of steel plate local buckling and lack of boundary element. For example, it has a wall strength of 860 kN at 4% drift, corresponding to a strength loss of about 7%. Strength degradation for Models B1 and B2 was limited, attributed to having boundary plates in these Models.

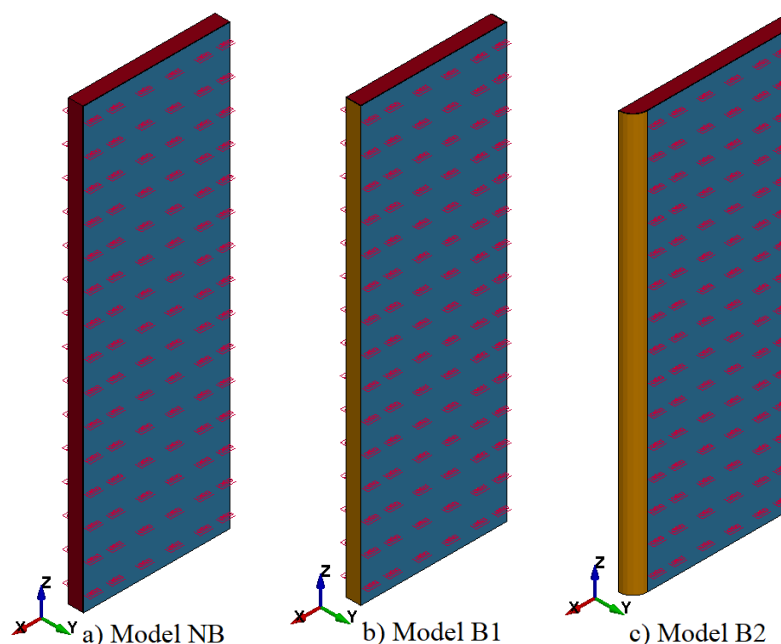


Fig. 3. Isometric views of the half-symmetric FE models of: (a) Model NB; (b) Model B1; and (c) Model B2.

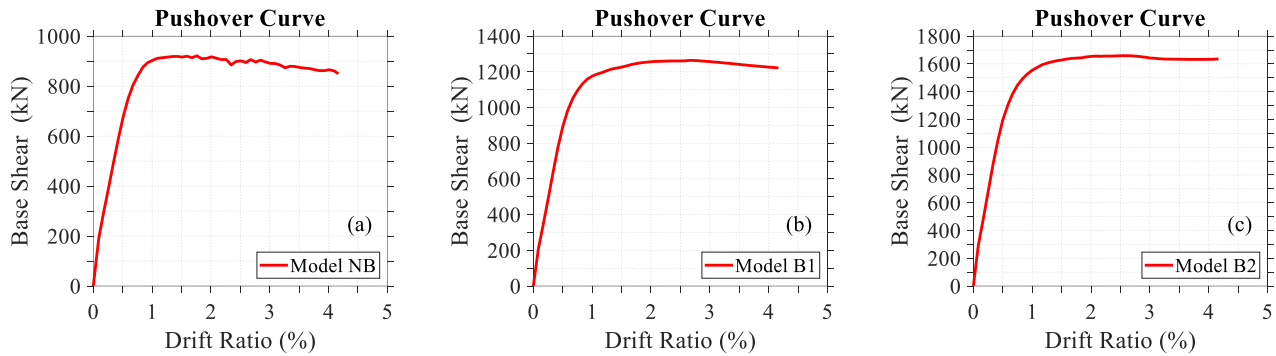


Fig. 4. Pushover curves of: (a) Model NB; (b) Model B1; and (c) Model B2.

3.3. Passive lateral pressure on boundary plates

Fig. 5(a-c) shows the contours of interface normal forces forming under flexural wall deformation for Models NB, B1 and B2. It should be noted that interface normal forces are nodal forces formed at the steel plate-concrete interface. Under wall flexure, the part of the concrete under compression expands laterally due to Poisson affect and shear dilation. The lateral expansion of concrete is restrained by the steel plates and tie bars which provides passive lateral pressure on concrete surface. Interfacial pressures can be obtained by first obtaining the interfacial normal forces at the interface nodes of steel plates then dividing these forces by the effective area. Therefore, the contours shown in the Figure can be interpreted as pressure contours other than the numerical values shown.

The highest values for passive lateral pressures occur in the region where the lateral expansion of the concrete is restrained by the tie bars and boundary plates. Tie bars provides lateral restraint by means of axial stiffness whereas boundary plates provide lateral restraints by means of transverse plate stiffness. Because Model NB has no boundary plate, tie bars located at the very bottom of the wall on the compression side were subjected to larger axial force demands. However, for Models B1 and B2, boundary plates contributed to transverse force resistance of the tie bars against concrete lateral expansion, so the tie bars of these Models received less axial force demands. Because of the round shape of the boundary plate of Model B2, the passive lateral pressures (or interface normal forces) were more evenly distributed, while lateral pressures were concentrated at the corner of the planar boundary plate of Model B1.

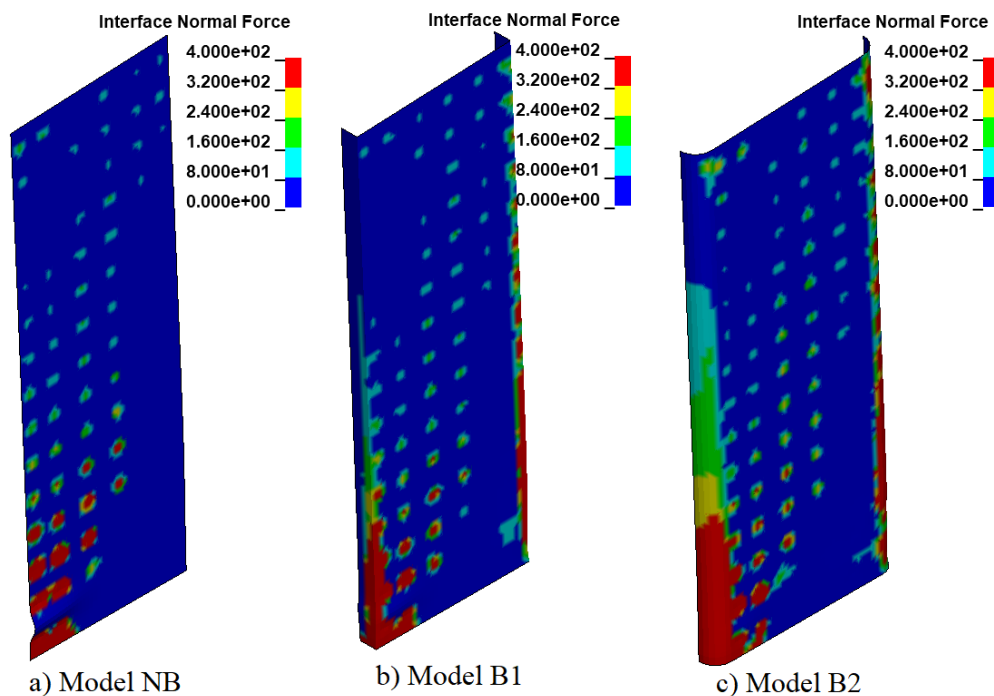


Fig. 5. Interface pressure acting on steel plate of: (a) Model NB; (b) Model B1; and (c) Model B2.

Although Fig. 5 provides useful information about the formation of passive lateral pressures, it cannot be interpreted reasonably for an understanding of the actual magnitude of the pressure distribution. To facilitate the

interpretation of the actual magnitude of pressure distribution, three-dimensional pressure distribution over a selected partial region of the boundary plates were plotted.

Fig. 6(a-b) shows these selected partial regions in Models B1 and B2 boundary plates. Fig. 7(a-b) shows the three-dimensional interface pressure distributions on the boundary plates of Models B1 and B2. Note that, interface pressures were obtained by dividing the interface force created at each node of the shell element by the corresponding tributary surface area of the element. As shown in Fig. 7(a), interface pressures reach their maximum where the planar boundary plate meets the web plate. The interface pressures decrease almost linearly from the maximum points and drop to zero at quarter wall thickness from the edge. As shown in Fig. 7(b), interface pressures are more evenly distributed over the interface area of the round boundary plate. Note that, slightly above the wall base, pressures drop in these areas as a result of plate local buckling in the round boundary plate. Compared to the pressure distribution on the

planar plate, the pressure distribution on the round plate is more uniform and is distributed higher elevation.

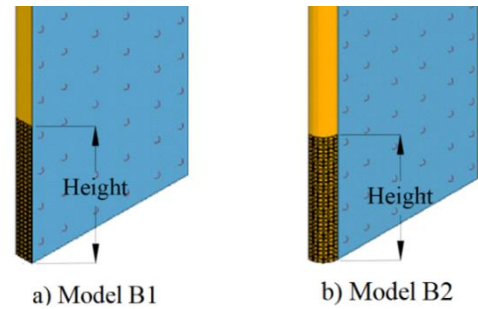


Fig. 6. Selected location of boundary plates of: (a) Model B1; and (b) Model B2 for 3D interface pressure distribution.

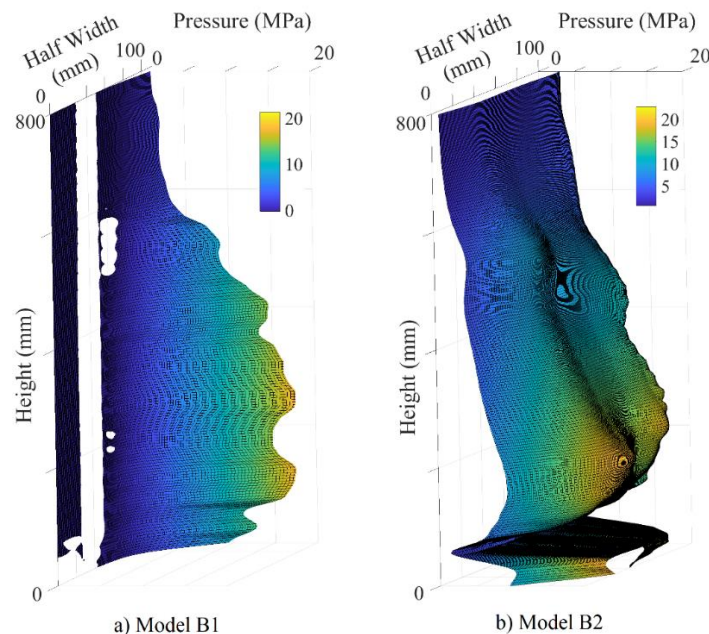


Fig. 7. 3D interface pressure distribution on boundary plates of: (a) Model B1; and (b) Model B2.

4. Comparison of Tie Bar Axial Forces

Fig. 8(a-f) compares axial force demands of the six tie bars (Tie_{11} , Tie_{12} , Tie_{21} , Tie_{22} , Tie_{31} , Tie_{32}) identified previously. For all Models, the tie bars closest to the wall boundary received larger axial force demands than the interior tie bars. This behavior is explained by the increase in concrete dilation as a result of increased axial strain demand on the concrete. Tie bars axial force demands decreased with distance from the wall base. Exception to this was observed in the second row of tie bars (i.e., Tie_{21} , Tie_{22}). For these bars, plate local buckling contributed to axial force demands (note that steel plate local buckling take place between the first and second row of tie bars). It should be noted that tie bars receive additional axial force demand due to prying action in addition to the confining action (Polat et al. 2021; Polat 2022). All the tie bars in Model NB received greater axial force demands than tie bars in Models B1 and B2. All the

tie bars in Models B1 and B2, except the first-row tie bars (i.e., Tie_{11} , Tie_{12}), received similar axial force demands. But for the first-row tie bars, the axial force demands in Model B1 are greater than in Model B2. This is attributed to the fact that the round boundary plate contribution to concrete confinement better than the planar plate. To demonstrate this, Fig. 9(a-b) shows the force variation in the transverse direction on the boundary plates along the wall height for Models B1 and B2. The transverse forces were obtained by multiplying the transverse stresses on the shell element with the area of the shell element in the transverse direction. Force demands were obtained at 0.5%, 1.0%, 2.0%, 3.0% and 4.0% wall drift ratios. For both Models, the transverse force demands on the boundary plates increase with increasing wall drift. For Model B2, the curves are smoother while for Model B1 they are slightly jagged. While transverse forces on the planar boundary plate were almost limited to a height of plastic hinge (1000mm) for Model B1,

transverse forces on the round boundary plate of Model B2 were spread out almost to the height of the wall. This is important in terms of showing the effectiveness of the round boundary plate compared to the planar one. Comparison of tie bars axial force demands for walls with and

without boundary plates in Fig. 8(a-f) demonstrate that the theoretical models developed by Polat (2022) based on walls without boundary plates to predict tie bar maximum force demands are conservative and can also be applied for walls with boundary plates.

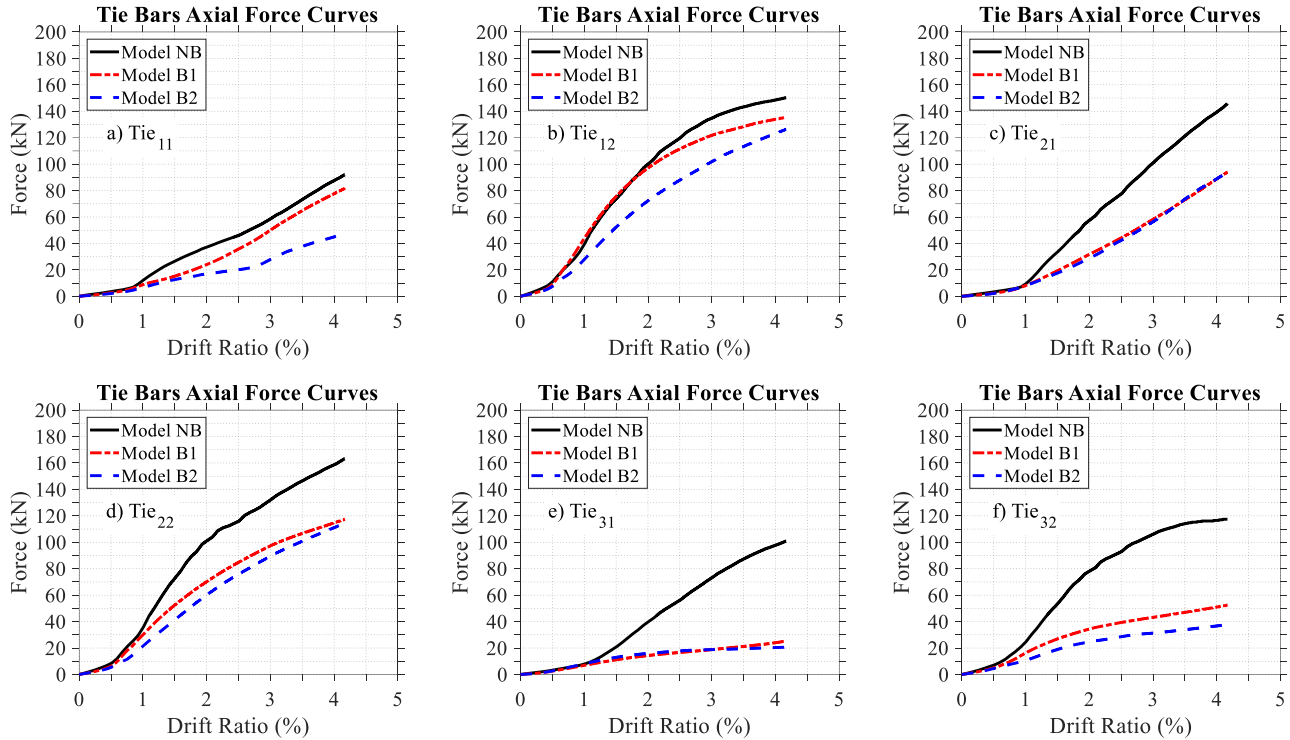


Fig. 8. Comparison of bar axial force demand in Models NB, B1 and B2 for: (a) Tie11; (b) Tie12; (c) Tie21; (d) Tie22; (e) Tie31; and (f) Tie32.

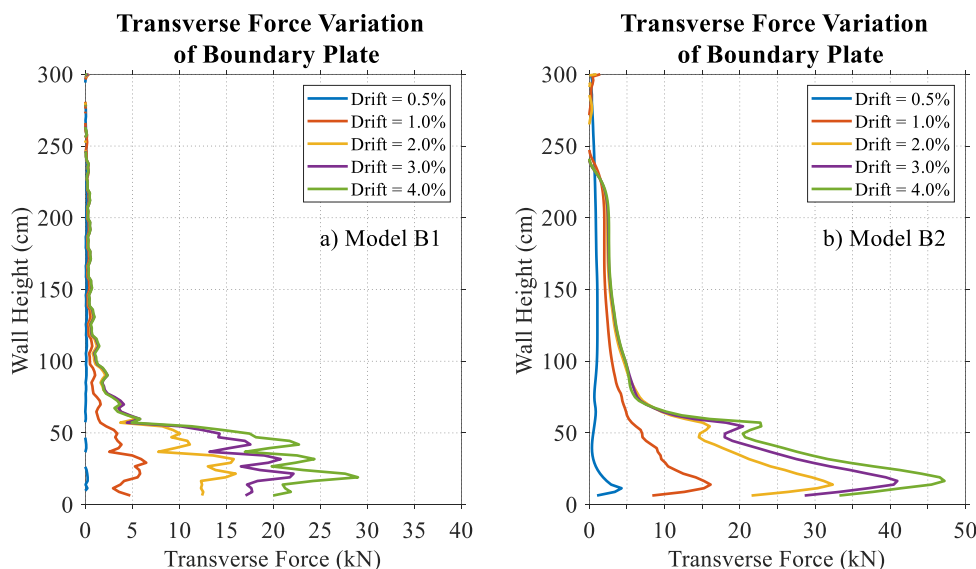


Fig. 9. Transverse force variation along the height of wall boundary elements: (a) Model B1; and (b) Model B2.

5. Conclusions

The influence of boundary plates on tie bar axial force demands in planar C-PSW/CF was numerically investigated. Three-dimensional finite element wall models

were developed. Three planar C-PSW/CF were used, two of which had boundary elements consisting of planar and round plates. The models were subjected to monotonic displacement up to 4% drift ratio. The findings from the numerical results are as follows:

- Inclusion of boundary plates resulted in a decrease in tie bars axial force demands. This applies to both types of boundary plates.
- Except for the tie bars located at the very bottom of the wall, the tie bars received almost similar axial force demands for both type of boundary plates.
- Compared to the wall without boundary plate, tie bar axial force demands in the walls with boundary plates decreased significantly with distance from the base of the wall.
- The theoretical models developed previously by Polat (2022) based on walls without boundary plates to predict tie bar maximum force demands are conservative and can also be applied for walls with boundary plates.
- Passive lateral pressures are more evenly distributed on the round plate but spread towards the corners on the planar plate. This is important for the connection between the boundary plates and the web plates. Pressure concentration on the plate corners may require more rigorous connection design between the boundary plates and web plates.
- The round boundary plate takes greater transverse force demands than the planar plate, especially contributing more to the confining force resistance of the first-row tie bars, thus helping to decrease force demands on these tie bars.

Acknowledgements

None declared.

Funding

The author received no financial support for the research, authorship, and/or publication of this manuscript.

Conflict of Interest

The author declared no potential conflicts of interest with respect to the research, authorship, and/or publication of this manuscript.

REFERENCES

- AISC (2022). Seismic provisions for structural steel buildings. AISC 341-22, American Institute of Steel Construction, Chicago, IL.
- Alzeni Y, Bruneau M (2014). Cyclic inelastic behavior of concrete filled sandwich panel walls subjected to in plane flexure. *Technical Rep. MCEER, 14-009*, Univ. at Buffalo, the State Univ. of New York, Buffalo, NY, MCEER.
- Alzeni Y, Bruneau M (2017). In-plane cyclic testing of concrete-filled sandwich steel panel walls with and without boundary elements. *Journal of Structural Engineering*, 143(9), 04017115.
- Bowerman H, Gough M, King C (1999). Bi-Steel Design and Construction Guide. British Steel Ltd, Scunthorpe, London.
- Eom T-S, Park H-G, Lee C-H, Kim J-H, Chang I-H (2009). Behavior of double skin composite wall subjected to in-plane cyclic loading. *Journal of Structural Engineering*, 135(10), 1239-1249.
- Kenarangi H, Kizilarslan E, Bruneau M (2021). Cyclic behavior of c-shaped composite plate shear walls—Concrete filled. *Engineering Structures*, 226, 111306.
- LSTC (2022). Livermore Software Technology Corporation, version R8.0. Livermore Software Technology Corporation, Livermore, CA.
- Oduyemi T, Wright H (1989). An experimental investigation into the behaviour of double-skin sandwich beams. *Journal of Constructional Steel Research*, 14(3), 197-220.
- Polat E (2020). Investigation of influence of concrete material models on cyclic inelastic response of a concrete filled composite plate shear wall. *Challenge Journal of Structural Mechanics*, 6(2), 91-98.
- Polat E (2022). Theoretical models for tie bar maximum axial force demand in composite plate shear walls—concrete filled. *International Journal of Steel Structures*, 22(4), 1108-1125.
- Polat E, Bruneau M (2017). Modeling cyclic inelastic in-plane flexural behavior of concrete filled sandwich steel panel walls. *Engineering Structures*, 148, 63-80.
- Polat E, Bruneau M (2018). Cyclic inelastic in-plane flexural behavior of concrete filled sandwich steel panel walls with different cross-section properties. *Engineering Journal, American Institute of Steel Construction*, 55, 45-76.
- Polat E, Kenarangi H, Bruneau M (2021). Investigation of tie bars axial force demands in composite plate shear walls—concrete filled. *International Journal of Steel Structures*, 21(3), 901-921.
- Ramesh S (2013). Behavior and design of earthquake-resistant dual-plate composite shear wall systems. Technical Report, Purdue University.
- Varma AH, Shafaei S, Klemencic R (2019). Steel modules of composite plate shear walls: Behavior, stability, and design. *Thin-Walled Structures*, 145, 106384.
- Wright H, Oduyemi T, Evans H (1991). The experimental behaviour of double skin composite elements. *Journal of Constructional Steel Research*, 19(2), 97-110.
- Xie M, Chapman J (2006). Developments in sandwich construction. *Journal of Constructional Steel Research*, 62(11), 1123-1133.